Antiviral Research 213 (2023) 105588

Contents lists available at ScienceDirect

Antiviral Research

journal homepage: www.elsevier.com/locate/antiviral

Importin α/β-dependent nuclear transport of human parvovirus B19 nonstructural protein 1 is essential for viral replication

Gualtiero Alvisi [a,*], Elisabetta Manaresi [b], Emily M. Cross [c], Mikayla Hoad [c], Nasim Akbari [a], Silvia Pavan [a], Daryl Ariawan [d], Gloria Bua [b], Gayle F. Petersen [c], Jade Forwood [c], Giorgio Gallinella [b]

[a] Department of Molecular Medicine, University of Padova, 35121, Padova, Italy
[b] Department of Pharmacy and Biotechnology, University of Bologna, 40138, Bologna, Italy
[c] School of Dentistry and Medical Sciences, Charles Sturt University, Wagga Wagga, NSW, 2650, Australia
[d] Dementia Research Centre, Macquarie University, Sydney, NSW, 2109, Australia

ARTICLE INFO

Keywords:
B19V
Nuclear transport
Antiviral
cNLS
Importins
Ivermectin

ABSTRACT

Human parvovirus B19 (B19V) is a major human pathogen causing a variety of diseases, characterized by a selective tropism to human progenitor cells in bone marrow. In similar fashion to all *Parvoviridae* members, the B19V ssDNA genome is replicated within the nucleus of infected cells through a process which involves both cellular and viral proteins. Among the latter, a crucial role is played by non-structural protein (NS)1, a multifunctional protein involved in genome replication and transcription, as well as modulation of host gene expression and function. Despite the localization of NS1 within the host cell nucleus during infection, little is known regarding the mechanism of its nuclear transport pathway. In this study we undertake structural, biophysical, and cellular approaches to characterize this process. Quantitative confocal laser scanning microscopy (CLSM), gel mobility shift, fluorescence polarization and crystallographic analysis identified a short sequence of amino acids (GACHAKKPRIT-182) as the classical nuclear localization signal (cNLS) responsible for nuclear import, mediated in an energy and importin (IMP) α/β-dependent fashion. Structure-guided mutagenesis of key residue K177 strongly impaired IMPα binding, nuclear import, and viral gene expression in a minigenome system. Further, treatment with ivermectin, an antiparasitic drug interfering with the IMPα/β dependent nuclear import pathway, inhibited NS1 nuclear accumulation and viral replication in infected UT7/Epo-S1 cells. Thus, NS1 nuclear transport is a potential target of therapeutic intervention against B19V induced disease.

1. Introduction

Human parvovirus B19 (B19V) is a human ubiquitous viral pathogen belonging to the Erythroparvovirus genus within the *Parvoviridae* family (Penzes et al., 2020; Qiu et al., 2017). B19V infects the majority of the human population at early age and is generally associated with fifth disease or *erythema infectiosum*, a mild, self-limiting childhood disease (Chorba et al., 1986), or arthropathies mainly in adults (White et al., 1985). Given the ability to infect and induce apoptosis in erythroid progenitor cells, infection of individuals with underlying immune or hematologic disorders can result in severe consequences, including both acute and chronic erythroid aplasia (Brown, 2000; White et al., 1985). Furthermore, fetal infection during pregnancy may result in hydrops fetalis and fetal death (Bonvicini et al., 2017a). Neither vaccines nor specific antivirals have been approved so far and therefore the identification of new targets of therapeutic intervention is of pivotal interest (Manaresi and Gallinella, 2019). B19V is a small, non-enveloped virus whose 5.6 Kb ssDNA genome contains an internal coding region, encoding at least five proteins, flanked by palindromic sequences capable of forming terminal hairpin structures and serving as the origin of replication. The best characterized viral-encoded polypeptides so far are the capsid proteins VP1 and VP2 (Cotmore et al., 1986), along with nonstructural (NS) protein 1 (Zou et al., 2018). B19V productive infection is almost exclusively restricted to actively replicating bone marrow and fetal liver-derived erythroid progenitor cells (EPCs) (Ozawa et al., 1986; Yaegashi et al., 1989), where it induces cell cycle arrest and apoptosis (Luo et al., 2013; Moffatt et al., 1998). This results in very limited options for studying its life cycle in cell culture, with human primary $CD36^{+}$ EPCs and the UT7/Epo-S1 cell line being the two most

* Corresponding author.
E-mail address: gualtiero.alvisi@unipd.it (G. Alvisi).

https://doi.org/10.1016/j.antiviral.2023.105588
Received 10 January 2023; Received in revised form 8 March 2023; Accepted 25 March 2023
Available online 28 March 2023

Abbreviations

B19V	Human parvovirus B19
NS	nonstructural protein
EPCs	erythroid progenitor cells
NE	nuclear envelope
NPC	nuclear pore complex
IMP	importin
NLS	nuclear localization signal
cNLS	classical NLS
MVM	minute virus of mice
PPV	porcine parvovirus
FBS	fetal bovine serum
DMEM	Dulbecco's Modified Eagle's Medium
IVM	ivermectin
PBS	phosphate buffered saline
wt	wildtype
CLSM	confocal laser scanning microscopy
RT	room temperature
Fn	nuclear fluorescence
Fc	cytoplasmic fluorescence
IBB	Importin-β binding
FITC	fluorescein isothiocyanate
SV40	Simian vacuolating virus 40
LTA	large tumor antigen

characterized systems (Bua et al., 2016; Morita et al., 2001; Wong et al., 2008). The current model hypothesizes that viral genome replication occurs in the nucleus of host cells via a rolling hairpin mechanism, which involves DNA damage repair, through the concerted action of the host cell machinery and viral protein NS1 (Zou et al., 2018; Berns, 1990), a 671 amino acid multifunctional protein with a molecular weight of 74 kDa. Similar to its orthologues present in other *Parvoviridae* members, B19V NS1 is endowed with helicase and endonuclease activities, the latter being responsible for nicking a conserved sequence in the viral genome, thereby initiating rolling hairpin replication, after binding to the origin of replication (Sanchez et al., 2016). Furthermore, NS1 can transactivate transcription from the unique B19V promoter, and is capable of arresting cell cycle progression and promoting apoptosis of infected cells (Luo et al., 2013; Moffatt et al., 1998; Morita et al., 2003; Raab et al., 2002; Wan et al., 2010), thus allowing efficient and sustained viral transcription and promoting the release of infectious viral particles from infected cells. Therefore, NS1 is absolutely required for B19V replication (Zhi et al., 2006).

According to its functions in viral genome replication and transcription, NS1 colocalizes with viral DNA and host cell S phase factors in viral DNA replication centers in B19V infected EPCs (Luo et al., 2011, 2013).

Eukaryotic cells are highly compartmentalized with the nucleus separated from the cytoplasm by the nuclear envelope (NE). In the NE, the outer nuclear membrane (ONM), is separated by a 40–50 nm perinuclear space from the inner nuclear membrane (INM), whose nuclear face is connected to a thin protein meshwork called the nuclear lamina. The only passage through the NE is through nuclear pore complexes (NPCs), which are embedded in the NE at sites where the INM and ONM are merged. NPCs are huge macromolecular machines which allow passive diffusion of small molecules, ions and proteins with a molecular weight below 40–60 kDa (Timney et al., 2016), and active transport of factors which need to be quickly imported into the nucleus, or whose molecular weight is not compatible with passive diffusion (Gorlich et al., 1995). Active nuclear import is a signal and energy-dependent process mediated by members of the importin (IMP) superfamily, whereby IMPβ1 or one of its several homologues recognizes specific sequences on the cargo protein, termed nuclear localization signals (NLSs), and mediates cargo translocation through the NPC and its release in the nucleoplasm upon binding with the small GTPase Ran (for a review see (Alvisi et al., 2013)). In the best characterized pathway, IMPβ1 recognizes basic NLSs through the adapter molecule IMPα (Conti et al., 1998). Such NLSs are therefore termed classical (c)NLSs and can be either monopartite or bipartite, depending on the number of basic clusters present, as well as their binding mode to IMPα (Lange et al., 2007). Monopartite cNLSs interact with a specific binding site on IMPα (the major binding site), which contains four main binding pockets for NLS aminoacidic side chains. On the other hand, in order to functionally interact with IMPα, bipartite cNLSs need to simultaneously bind to the IMPα minor binding site, which contains two main pockets to accommodate amino acid side chains, thus lowering the Kd of the interaction (Fontes et al., 2000, 2003).

Given its molecular weight of 74 kDa, B19V NS1 needs to be actively translocated into the nucleus to perform its functions during the viral replication cycle, similarly to NS1 from other mammalian parvoviruses. Indeed, bipartite cNLSs have been identified within NS1 from minute virus of mice (MVM: **KK**DYT**K**CVLFGNMIAYYFLT**KKK**I-216, see Fig. 1C) and porcine parvovirus (PPV: **K**PETVETTVTTAQEA**KRG**R-274, see Fig. 1C), as essential for nuclear import (Cao et al., 2022; Ihalainen et al., 2007). Therefore, characterization of NS1 nuclear import pathway is crucial for our understanding of the biology and pathogenesis of B19V infection, with important implications for the development of highly-needed antivirals.

Although the K177C substitution has been shown to abrogate B19V NS1 nuclear import in transient transfection assays, a functional NS1 NLS has not been yet identified. Furthermore, the NS1 nuclear transport pathway and its role in the viral replication cycle have not been characterized (Cao et al., 2022; Nuesch and Tattersall, 1993; Wan et al., 2010). Here, we addressed such issues by combining genetics, bioinformatics, biochemical, structural, and microscopic analyses. Our results indicate that B19V NS1 possesses a monopartite cNLS located at amino acids 172–182, capable of mediating high affinity binding to the IMPα major binding site, and thus conferring nuclear localization to heterologous proteins and full length NS1. Inhibition of the IMPα/β-dependent nuclear import pathway impaired NS1 nuclear targeting and viral replication in infected UT7/Epo-S1 cells. Substitution of K177, which interacts with IMPα at the P2 position within the cNLS major binding site, severely impaired the NS1-IMPα interaction and nuclear targeting, and strongly inhibited viral genome amplification/transcription in a minigenome replicon system (Reggiani et al., 2022) in the absence of expression of structural proteins. Thus, NS1 nuclear transport could represent a potential target of antiviral intervention against B19V.

2. Materials and methods

2.1. Bioinformatics analysis

The sequence of B19V proteins was downloaded from UniProt (2021) using the B19V reference proteome (Uniprot code: UP000006624). The presence of putative cNLSs was predicted using the cNLS mapper software (Kosugi et al., 2009). The sequences of NS1 proteins from B19V, minute virus of mice (MVM), and porcine parvovirus (PPV), were retrieved from UniProt (UniProt codes: Q9PZT1, P03134, and P52502, respectively) and aligned using the Clustal Omega Multiple Sequence Alignment tool (Sievers et al., 2011), with Clustal W with character counts as output, and showing the Neighbour-joining tree without distance corrections and real branch length.

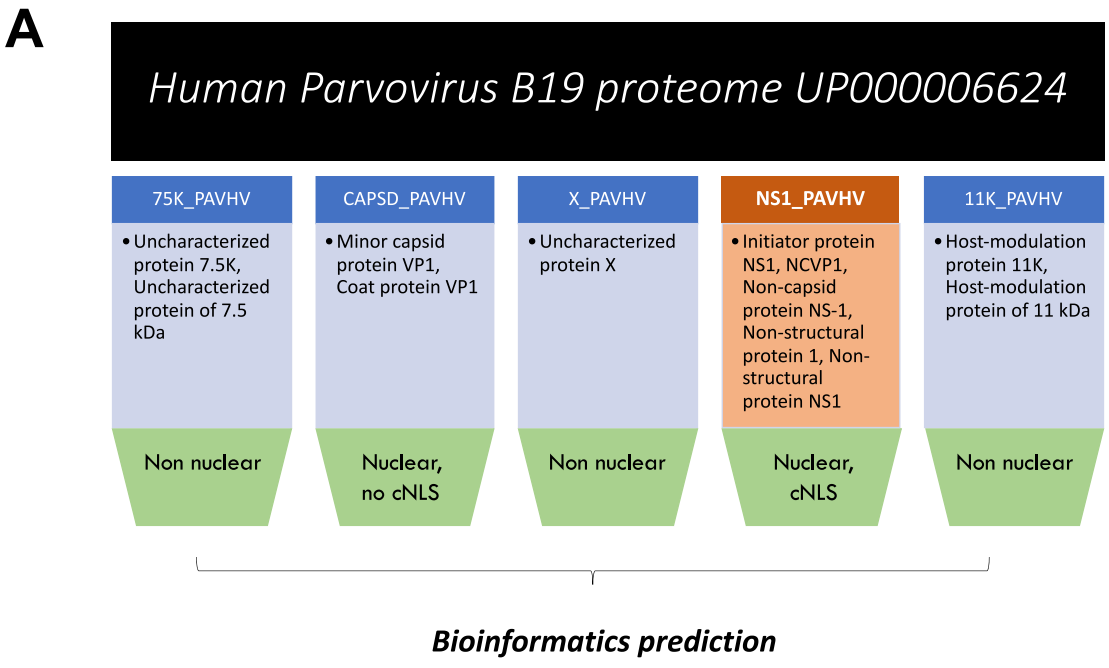

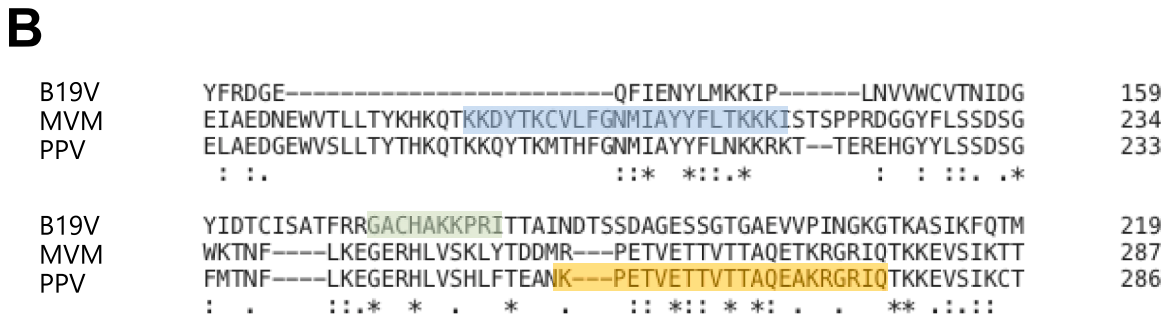

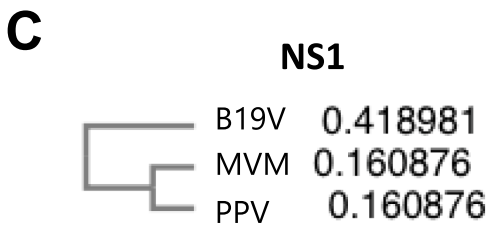

Fig. 1. B19V NS1 is predicted to translocate to the nucleus via the IMPα/β heterodimer using a cNLS located at residues 172–182. (A) The B19V reference proteome (Uniprot code: UP000006624) was retrieved from Uniprot and bioinformatically analyzed by combining Uniprot subcellular localization information with cNLS prediction software results, as described in the Materials and Methods. (B) The sequences of NS1 proteins from human parvovirus B19 (B19V, Uniprot code: Q9PZT1), minute virus of mice (MVM, Uniprot code: P03134) and porcine parvovirus (PPV, Uniprot code: P52502) were aligned with clustal Omega, as described in the Materials and Methods. The aligned primary sequence of each NS1 protein is shown with the single letter amino acid code, with previously described and putative cNLSs highlighted (previously described cNLS from MVM NS1, *pale blue*; putative cNLS from B19V B19 NS1, *green*; previously described cNLS from PPV NS1, *yellow*). (C) The Phylogram relative to NS1 from B19V, MVM and PPV is shown, along with indication of real branch length.

2.2. Oligonucleotides

Oligonucleotides (ThermoFisher Scientific, Monza, Italy) were resuspended in 10 mM Tris buffer (pH. 7.8) to a 100 μM final concentration and stored at −20 °C until needed, as described previously (Ghassabian et al., 2021). A list of all oligonucleotides used in this study is available in Supplementary Table I.

2.3. Plasmids

Plasmids pEGFP-N1-H1E and pEPI-GFP-human cytomegalovirus (HCMV)-UL44, encoding control GFP fusion proteins localizing to the nucleus via IMPα/β independent and dependent pathways, respectively (Alvisi et al., 2005, 2006a, 2008; Gerlitz et al., 2007). Plasmid mcherry-Bimax2, encoding a competitive inhibitor of the IMPα/β nuclear import pathway (Tsujii et al., 2015), was a generous gift from Yoshihiro Yoneda and Masahiro Oka (Osaka, Japan).

Plasmid pEGFPC1-B19V-NS1, encoding for a fusion protein between eGFP and B19V NS1 (Uniprot code: Q9PZT1), was synthesized by Bio-Fab Research (Rome, Italy). Plasmid pEGFPC1-B19V-NS1; K177T, encoding for an NLS defective substitution derivative thereof was generated via the Quikchange Lightning Mutagenesis kit (#210515,

Agilent Technologies, Cernusco sul Naviglio (MI), Italy) according to the manufacturer's recommendation, using oligonucleotides a530c_KY940273F and a530c_KY940273R and plasmid pEGFPC1-B19V-NS1 as a template, as described previously (Trevisan et al., 2018). Mammalian expression plasmids encoding for cNLSs fused to the C-terminus of cycle 3 GFP were generated using the NT-GFP Fusion TOPO™ Expression kit (#K481001, ThermoFisher Scientific, Monza, Italy), according to the manufacturer's recommendations with slight modifications. Briefly, appropriate oligonucleotide pairs (8.2 nM in TE buffer) were incubated at 95 °C for 5 min and then gradually cooled at room temperature (RT) to obtain DNA duplexes containing 3′ overhangs. cDNAs were cloned into plasmid pcDNA3.1-NT-GFP-TOPO. Reactions were performed by mixing 1 μl of duplex, 1 μl of salt solution [diluted 1:2 (v/v) in TE buffer], and 1 μl of pcDNA3.1-NT-GFP-TOPO vector [diluted 1:3 (v/v) in TE buffer]. All plasmids were verified by Sanger sequencing (BMR Genomics, Padova, Italy). The B19V minigenome (pCH10 pAs1) was previously described (Reggiani et al., 2022). A list of all plasmids used in this study is available in Supplementary Table II.

2.4. Chemicals

Ivermectin (IVM; #8898, Sigma, Merck Millipore, Milan, Italy) was resuspended in DMSO at a final concentration of 50 mM and stored in aliquots at −80 °C until needed.

2.5. Cells

HEK293A cells were propagated as described previously (Di Antonio et al., 2021). Briefly, cells were maintained in Dulbecco's Modified Eagle's Medium (DMEM) supplemented with 10% (v/v) fetal bovine serum (FBS), 50 U/ml penicillin, 50 U/ml streptomycin, and 2 mM L-glutamine in a humidified incubator at 37 °C in the presence of 5% CO_2, and passaged when confluence was reached. UT7/Epo-S1 cells were cultured in Iscove's Modified Dulbecco's Medium (IMDM), supplemented with 10% FBS and 2 U/mL rhu erythropoietin in a humidified incubator at 37 °C in the presence of 5% CO_2 (Bua et al., 2016). UT7/Epo-S1 cells were kept in culture at densities between 2×10^5-1×10^6 cells/ml, and used for infection and transfection experiments when at a density of 3×10^5 cells/ml.

2.6. Cell viability assay

The effect of IVM on cell viability was monitored by a WST-8 based assay, a water-soluble salt reagent that produces a formazan dye upon reduction in response to metabolic activity (CCK8 assay, Dojindo Molecular Technologies, Munich, Germany), following established and optimized protocols (Bonvicini et al., 2017b). For experiments, 5×10^4 UT7/Epo-S1 cells were seeded in 100 μL volumes in a 96-well plate, and cultured in the absence or presence of different concentrations of IVM. WST-8 reagent was added for the last 2 h of cell culture. The amount of formazan the dye was measured as absorbance (OD) values,1 according to the manufacturer's instructions. Replicate net OD values were normalized with respect to the control samples and expressed as mean percentage values for cell viability.

2.7. Infections

B19V was obtained from a cloned synthetic genome, as described (Manaresi et al., 2017). For infection, UT7/Epo-S1 cells were incubated in phosphate buffered saline (PBS) at a density of 1×10^7 cells/ml, in the presence of B19V at a multiplicity of infection of 10^3 genome equivalents (geq)/cell. Following 2 h at 37 °C, cells were washed twice in PBS to remove inoculum virus and incubated at 37 °C in 5% CO_2 in complete growth medium, at an initial density of 1×10^6 cells/ml. For investigation of IVM activity, UT7/Epo-S1 cells were cultured for 6 h in complete growth medium supplemented with different concentrations of IVM, then washed in PBS, infected as described, and cultured for a further 48 h in the presence of IVM.

2.8. Nucleic acids purification

Equal amounts of cell cultures, corresponding to $1x10^5$ cells, were collected as appropriate at 2h or 48 h post infection and processed using the Maxwell Viral Total Nucleic Acid kit (#AS1330, Promega Italia, Milan, Italy) on a Maxwell MDx platform (Promega Italia, Milan, Italy), following the manufacturer's instructions, in order to obtain a total nucleic acid fraction in an elution volume of 100 μL.

2.9. Quantitative real-time PCR and RT-PCR

For the analysis of B19V DNA, aliquots of the eluted nucleic acids (corresponding to ~500 cells) were directly amplified in a qPCR assay (Maxima SYBR Green qPCR Master Mix, ThermoFisher Scientific, Monza, Italy). For the analysis of B19V RNA (total RNA and NS RNA), aliquots of the eluted nucleic acids (corresponding to ~500 cells) were first treated with Turbo DNAfree reagent (ThermoFisher Scientific, Monza, Italy) before amplification in a qRT-PCR assay (QuantiNova SYBRGreen RT-PCR kit, Qiagen, Milan, Italy). Standard cycling programs were used, followed by a melting curve analysis to define the Tm of amplified products. Genomic DNA coding for 18S rRNA (rDNA) was amplified for calibration with respect to cell copy number. Primer pairs were selected to allow quantitation of viral DNA, total RNA, and NS RNA (Supplementary Table II). Quantitative evaluation of target was obtained by absolute quantitation on external calibration curves as described (Bonvicini et al., 2008).

2.10. Transfections

HEK293A cells were seeded onto glass coverslips in a 24-well plate (5×10^4 cells/well). The next day, cells were transfected with appropriate amounts of expression constructs (range 5–250 ng) using Lipofectamine 2000 (ThermoFisher Scientific, Monza, Italy), following the manufacturer's recommendations and further incubated in complete growth medium at 37 °C and 5% CO_2, as described previously (Sinigalia et al., 2008), until being processed for confocal laser scanning microscopy (CLSM). UT7/Epo-S1 cells were transfected with B19V minigenome pCH10 pAs1-derived PCR products (see below) using the Amaxa Nucleofection System (Lonza, Basel, Switzerland), with V Nucleofector Reagent and T20 program setting, at a ratio of 1 μg insert DNA for 1×10^6 cells. Following transfection, the cells were incubated in complete growth medium at 37 °C and 5% CO_2 at an initial density of 1×10^6 cells/ml. Constant amounts of cell cultures were collected at 6 h, 24 h and 48 h post-transfection. Cells and cell-free supernatants were separated by centrifugation at 5000 rpm for 5 min, then used for analysis and successive experiments.

2.11. Preparation of B19V minigenome pCH10 pAs1-derived PCR products

For transfection, DNA inserts were generated by recombinant PCR using pCH10 pAs1 template. Wildtype (wt) DNA was generated in single PCR round using primers HH0 and HH1. K177T DNA, mediating the expression of NS1 protein bearing the K177T substitution and thus inactivating its cNLS, was generated in two rounds; in the first, two segments were obtained using the primer pairs HH1-NLS K177R R and NLS K177R F-HH0, and in the second, a unique segment was obtained using the external primer pair HH1-HH0. NS1KO, whereby expression of full length NS1 is prevented by substituting the ATG sequence with TAA was similarly constructed, by using primers NS1 KO F and NS1 KO R as internal primers in the first round. Amplification was carried out by using the High-Fidelity PCR System (Merck Life Science, Milan, Italy),

according to manufacturer's instructions, with a thermal profile consisting of: initial denaturation 94 °C, 2 min; 10 cycles of denaturation 94 °C, 15 s, annealing 50 °C, 30 s, extension 72 °C, 2 min 30 s; 20 cycles of denaturation 94 °C, 15 s, annealing 50 °C, 30 s, extension 72 °C, 2 min 30 s incremented by 5 s/cycle; final extension 72 °C, 7 min. Following agarose gel electrophoresis analysis, amplification products were purified by using the Wizard® SV Gel and PCR Clean-Up System kit (#A9281, Promega Italia, Milan, Italy), and quantified by the Qubit 2.0 Fluorometer (Promega Italia, Milan, Italy). Amplified products were confirmed by sequencing (Eurofins Genomics, Ebersberg, Germany) before transfection.

2.12. Confocal laser scanning microscopy (CLSM) and image analysis

For detection of viral proteins by immunofluorescence, $5x10^4$ UT7/Epo-S1 cells were spotted on glass slides and fixed with 1:1 acetone: methanol for 10 min at −20 °C. For detection of NS protein, cells were incubated with the human monoclonal antibody MAb1424 (#94408, Mikrogen Diagnostik, Neuried, Germany; 1:100 in PBS/FBS 10%), then with an α-human Alexa Fluor 488-conjugated secondary antibody (#A-11013, ThermoFisher Scientific, Monza, Italy; 1:200 in PBS/FBS 10%). Nuclei were stained with DRAQ5 (#62251, ThermoFisher Scientific, Monza, Italy; 1:5000 in PBS/BSA 1%) and Hoechst 33342 (#H3570, ThermoFisher Scientific, Monza, Italy; 1:10000 in PBS/BSA 1%), while actin filaments were stained with FITC-phalloidin (#P5282, Sigma, Merck Millipore, Milan, Italy; 1:50 in PBS/BSA 1%). The number of positive cells was analyzed using a DM IL LED Leica epifluorescence microscope equipped with 10x and 20× objectives, appropriate filter cubes and a DFC 7000 T digital camera (Leica, Heidelberg, Germany), while subcellular localization of NS1 was investigated using a Nikon A1 confocal laser scanning microscope equipped with a 60× oil immersion objective (Nikon, Tokio, Japan) as described previously (Alvisi et al., 2018). For detection of spontaneously fluorescent proteins 48 h post transfection, cells were incubated for 30 min with DRAQ5 (#62251, ThermoFisher Scientific, Monza, Italy; 1:5000 in DMEM no phenol red) washed with PHEM 1x (60 mM PIPES, 25 mM HEPES, 10 mM EGTA, and 4 mM $MgSO_4$) and fixed with paraformaldehyde/PHEM 3% (v/v) for 10 min at RT. Following three washes with PHEM 1x and one wash with milliQ water, coverslips were mounted on glass slides with Fluoromount G (Southern Biotech, Birmingham, AL, USA). Intracellular ATP was depleted by incubating cells for 30 min at 37 °C in DMEM containing no glucose, 5% FBS, and supplemented with 10 mmol/L sodium azide, 6 mmol/L 2-deoxy-D-glucose (D8357, Sigma, Merck Millipore, Milan, Italy) and DRAQ5 (#62251, ThermoFisher Scientific, Monza, Italy; 1:5000) before sample processing as described above. Subcellular localization of fusion proteins was analyzed using a Nikon A1 confocal laser scanning microscope equipped with a 60× oil immersion objective (Nikon, Tokio, Japan) as described previously (Alvisi et al., 2018).

2.13. Image analysis

Levels of nuclear accumulation of proteins of interest were determined using the FiJi public domain software (https://doi.org/10.1038/nmeth.2019) and single cell measurements for each of the nuclear (Fn) and cytoplasmic (Fc) fluorescence, subsequent to the subtraction of fluorescence due to autofluorescence/background as described previously (Alvisi et al., 2006a).

2.14. Protein purification and peptide synthesis

The IMPα2 (UniProtKB P52293) the mouse hortologue of human IMPα1 (KPNA2), was used for structure determination and binding assays in this study. A plasmid containing the gene corresponding to the N-terminally truncated IMPα2 lacking the autoinhibitory IMPβ binding (IBB) domain (IMPα2ΔIBB, residues 71–529) with a 6x histidine tag in the pET30 expression vector was transformed into BL21 (DE3) pLysS *E. coli* cells and expressed using the auto-induction method for 24 h at RT (Studier, 2005). Following harvesting of the whole cells and resuspension in Buffer A (50 mM phosphate buffer pH 8.0, 300 mM NaCl, 20 mM imidazole), cells were lysed by three freeze-thaw cycles, treated with lysozyme and DNAse, incubated for 45 min, then centrifuged at 12, 000 rpm to collect the soluble extract and remove cell debris. The soluble extract was further clarified using a 0.22 μm syringe filter then injected over a 5 mL Ni-Sepharose HisTrap HP column (Cytiva, Marlborough, USA). The bound sample was washed with 10 column volumes of Buffer A, then eluted using a gradient of Buffer B (50 mM phosphate buffer pH 8.0, 300 mM NaCl, 500 mM imidazole) over 5 column volumes. Peak fractions were pooled and subsequently purified over gel filtration using a Superdex 200 26/60 column (Cytiva, Marlborough, USA) and Buffer C (50 mM Tris pH 8.0, 125 mM NaCl). Peak fractions were pooled, concentrated using 10 KDa molecular weight centrifugal filters (Merck Millipore, Milan, Italy), and stored at −80 °C for further use. N-terminally fluorescein isothiocyanate (FITC)-tagged peptides corresponding to the B19V NS1 NLS region (GACHAKKPRIT-182) and mutant variants were synthesized using an automated CEM Liberty Blue solid phase peptide synthesizer. The coupling reaction was performed with DIC and Oxyma coupling reagent at 90 C. Fmoc deprotection was performed at 90 C using 20% (v/v) piperidine/DMF solution. After the last coupling, the peptide was cleaved from the resin with a solution of TFA/TIPS/H_2O (95/2.5/2.5) for 3 h. Peptide residue was purified using HPLC and lyophilized to powder.

2.15. Gel mobility shift assays

To confirm the interaction between IMPα2ΔIBB and B19V NLS peptides, electrophoresis mobility shift assays (EMSAs) were carried out using 10 μM FITC-tagged NLS peptide (wt, K177T mutant, or K178T mutant) and 20 μM bacterially expressed IMPα2ΔIBB on a 1.5% agarose gel in TB buffer (0.45 mM Tris base, 0.45 mM boric acid, pH 8.5). Simian vacuolating virus 40-large tumor antigen (SV40-LTA) NLS and IMPα2ΔIBB alone controls were also run. Gels were first imaged using a UV filter to detect FITC-peptide, then treated with Coomassie to stain and observe protein bands. The assay was repeated in triplicate.

2.16. Fluorescence polarization assays

To assess the binding affinity of the B19V NLS to IMPα2ΔIBB, fluorescence polarization assays were performed using FITC-tagged NLS peptides (wt, K177T mutant, or K178T mutant) and bacterially expressed IMPα2ΔIBB. A positive control using the SV40-LTA NLS and IMPα2ΔIBB was also measured. Two-fold dilutions of 30 μM IMPα2ΔIBB was titrated across 23 wells of a black Fluotrac microplate (Greiner Bio-One, Kremsmünster, Austria) and 10 nM FITC-peptide was added to each well. The final volume per well was 200 μL, using Tris buffered saline, pH 8.0. A control containing no IMPα2ΔIBB was also prepared and used for gain adjustment. Fluorescence polarization measurements were immediately recorded using a CLARIOstar Plus plate reader (BMG Labtech, Mornington, Australia) and the assay was repeated in triplicate for each peptide. One site specific binding least square fit curves were plotted using GraphPad Prism 9.0 (GraphPad, San Diego, CA, USA).

2.17. Crystallization of NLS peptides complexed with IMPα2ΔIBB

Crystallization used hanging-drop vapor diffusion where a 1.5 μL stock containing a molar ratio of 3:1 peptide:protein was mixed with 1.5 μL of reservoir solution and suspended over a 300 μL reservoir well. Crystals (grown in 0.70 M sodium citrate, 0.1 M HEPES, 0.01 M DTT, pH 6.5) were harvested, treated with a cryoprotectant containing the reservoir solution and 20% glycerol, then flash cooled in liquid nitrogen. Crystals were diffracted using the MX2 beamline at the Australian Synchrotron (Aragao et al., 2018). Data collected was auto-processed with XDS for integration and scaling (Kabsch, 2010). Within the CCP4

suite, Aimless was used for merging and selection of 5% R_{free} (Evans, et al., 2013). Cycles of refinement using Phenix Refine and model building using Coot were employed until a final structure was achieved (Adams et al., 2010; Emsley et al., 2010). The structure was deposited in the PDB under the accession code 8F2Q.

2.18. Statistical analysis

Data were statistically analyzed by performing either Student's *t*-test, one way, or two-way ANOVA using GraphPad Prism 9 software (GraphPad, San Diego, CA, USA).

3. Results

3.1. B19V NS1 mainly localizes to the nucleus of infected cells

Since pharmacological inhibition of the IMPα/β heterodimer-dependent nuclear import pathway impairs the replication of different human viruses (Cao et al., 2022; Lv et al., 2018; Mastrangelo et al., 2012; Raza et al., 2020; Xu et al., 2018; Yang et al., 2020), we bioinformatically analyzed the B19V proteome (Uniprot ID: UP000006624) for the presence of proteins likely imported into the nucleus using such a pathway (Fig. 1A). Among the five proteins retrieved, only NS1 (Uniprot code: Q9PZT1) was predicted to possess a putative classical nuclear localization signal (cNLS) according to cNLS mapper (GACHA**KKPR**IT-182). Further, despite VP1 having been detected in the cell nuclei, it does not display a motif resembling a cNLS (Deng et al., 2013). We hypothesized that the putative cNLS identified here could be responsible for NS1 nuclear targeting via the IMPα/β heterodimer. Whilst cNLSs for NS1 from other mammalian parvoviruses have been described (MVM NS1: **KK**DYT**K**CVLFGN-MIAYYFLT**KKK**I-216; PPV NS1: **K**PETVETTVTTAQEA**KR**G**R**-274), these signals are bipartite in nature and are not conserved within the B19V NS1 amino acid sequence. The B19V NS1 putative cNLS (GACHA**KK-PR**IT-182) is similarly not conserved in MVM and PPV NS1 (Fig. 1B), suggesting cNLSs have evolved independently during parvovirus evolution. Indeed, NS1 from MVM and PPV are phylogenetically closer (branch length 0.16) compared to NS1 from B19V (branch length 0.42, see Fig. 1C).

We initially analyzed the subcellular localization of NS1 at different

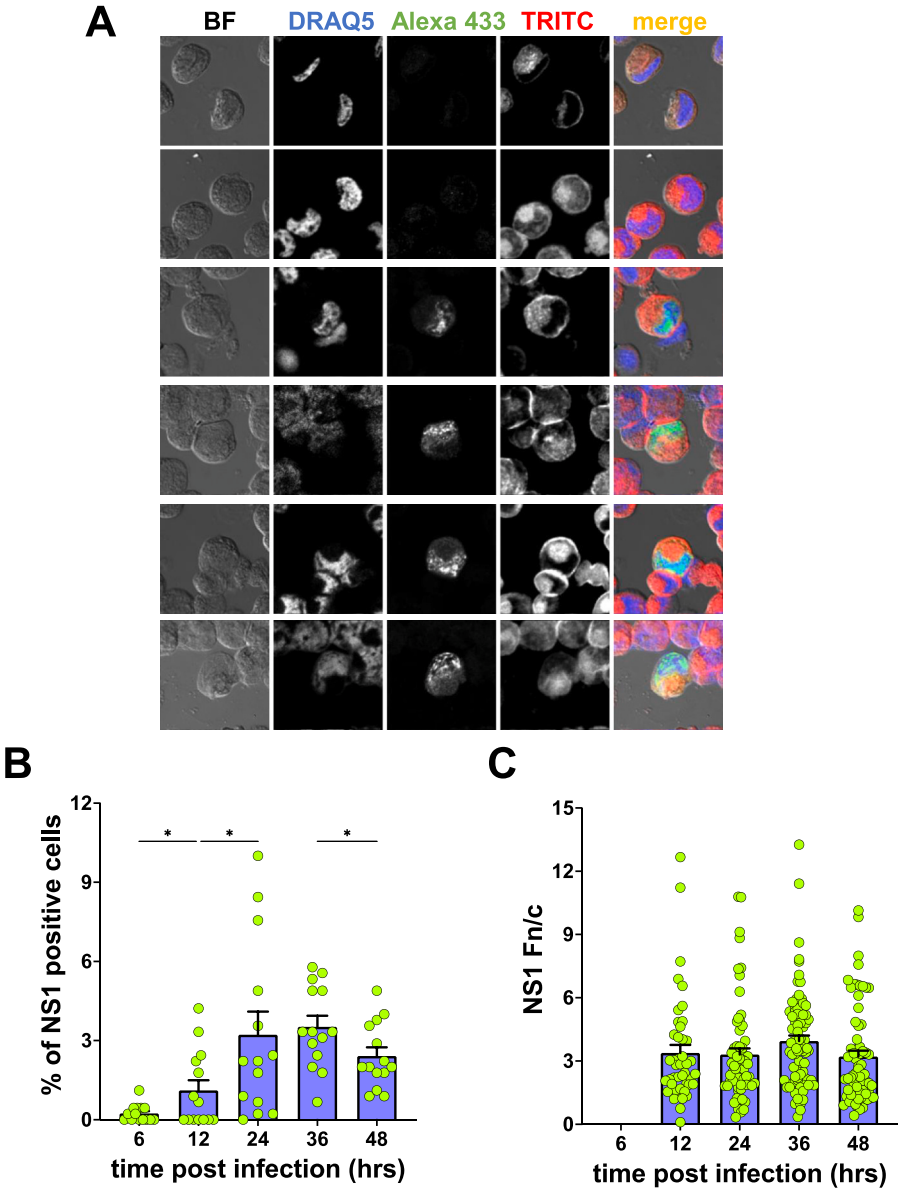

Fig. 2. NS1 localizes in the cell nucleus during B19V infection. UT7/Epo-S1 cells were either infected with B19V or mock infected. At the indicated time points post infection, cells were harvested and processed as described in the Materials and Methods to enable microscopic detection of cell nuclei by staining with DRAQ5, NS1 by incubation with a monoclonal antibody followed by incubation with a secondary antibody conjugated to Alexa Fluor 488, and actin filaments by staining with TRITC-phalloidin. Samples were then analyzed with a Leica epilfluorescence microscope equipped with a 20× objective, and with a Nikon A1 confocal laser microscope equipped with a 60× oil immersion objective (A) to count the number of positive cells (B) and to quantitatively analyze the levels of nuclear accumulation at the single cell level (C). (A) Representative images of the brightfield (BF), cell nuclei (DRAQ5), NS1 (Alexa 488) and actin filaments (TRITC) relative to randomly chosen fields are shown, along with merged images in the *right* panels. (B) Percentages of NS1 positive cells relative to seven fields each from three independent experiments are shown as individual measurements, means and standard deviation (SD) of the mean, along with the results of Brown-Forsythe and Welch ANOVA tests. *: $p < 0.05$. (C) The levels of nuclear accumulation of NS1 (Fn/c ratios) of single cells relative to six fields each from three independent experiments are shown as individual measurements, means and SD of the mean, along with the results of Brown-Forsythe and Welch ANOVA tests.

times post infection of UT7/Epo-S1 cells, quantifying the levels of nuclear accumulation by CLSM. Our data indicate that NS1 became detectable at very low levels starting at 6 h post infection (Fig. 2AB). The number of NS1 positive cells peaked at 24–36h post infection (~3% of cells, see Fig. 2AB), and quantitative confocal laser scanning microscopy (CLSM) analysis revealed that NS1 accumulated in the nucleus of infected cells at each time post infection (Fn/c ~ 3, see Fig. 2C). Given that the c. 74 kDa molecular weight of B19V NS1 is well above the cut-off for passive diffusion across the NPC, its nuclear localization suggests that it needs to be actively transported inside the host cell nucleus during viral infection.

3.2. *B19V NS1 residues 172–182 bind to IMPα2 in the major binding site and represent a functional monopartite cNLS*

We therefore decided to investigate the ability of NS1 residues 172–182 to form a complex with the nuclear transporter IMPα2. To this end, we pursued structural analysis of the B19V NS1(172–182)-IMPα2 interaction. The N-terminally truncated mouse IMPα2 lacking the autoinhibitory IMPβ Binding (IBB domain), IMPα2ΔIBB, was used for crystal trials with FITC-tagged B19V NS1(172–182) peptide. Following co-crystallization, crystals were diffracted at the Australian Synchrotron on the MX2 beamline, and the structure was refined to a resolution of 2.7 Å with model quality represented by an overall R_{work} and R_{free} of 21.49% and 22.84%, respectively (see Supplementary Table III for full data collection and refinement statistics). The IMPα2ΔIBB structure (elucidated for residues 72–496) shows the central IMPα2 domain comprised of ten tandem Armadillo Repeats (ARMS 1–10) and a conserved concave binding region (Fig. 3A). Electron density for the IMPα polyhistidine expression tag and peptide FITC-label were not discernible, and were therefore omitted from the model.

In our structure, we have modelled two monopartite cNLS peptides running antiparallel to IMPα2 at the major (located at ARMS 2–4, interface area of 650.8 $Å^2$) and minor (located at ARMS 6–8, interface area of 527.8 $Å^2$) binding sites (Fig. 3A). The B19V NS1 cNLS peptides bind similarly at both sites, involving residues K175-R180, with slightly extended binding (including C174 and I181) at the major site (Fig. 3AC). Structural alignment indicates that B19V NS1(172–182) binds to IMPα2 in a similar fashion to the well-established and extensively studied SV40-LTA cNLS (PDB: 1EJL, Fig. 3B).

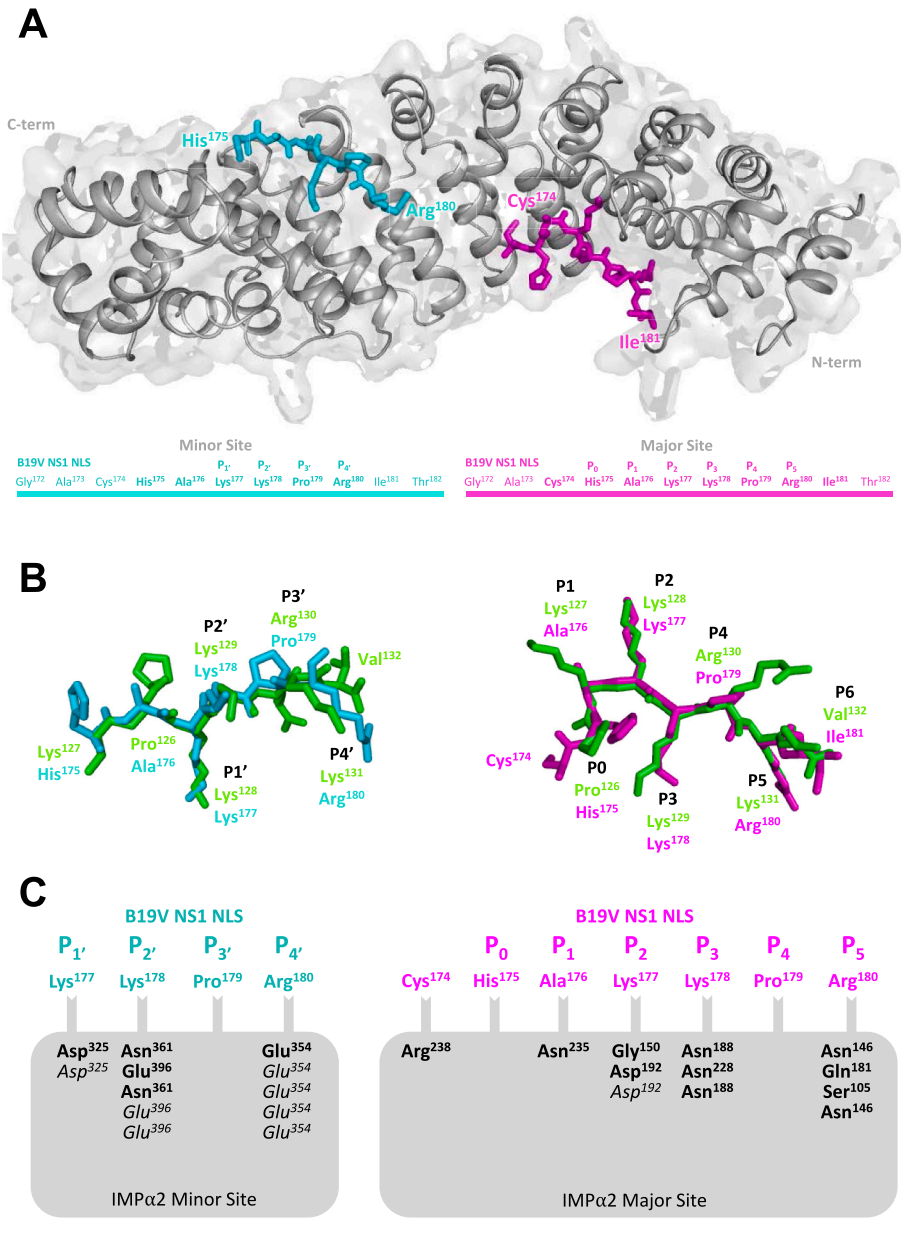

Fig. 3. Crystal structure of the B19V NS1 cNLS: IMPα2ΔIBB complex. (A) Crystal structure of B19V NS1 cNLS:IMPα2ΔIBB. *Silver* indicates IMPα2ΔIBB, *cyan* is the minor site bound B19V NS1 cNLS, and *magenta* is the major site bound B19V NS1 cNLS. (B) Structural alignment of B19V NS1 cNLS at the major site (*magenta*) and minor site (*cyan*) compared to the SV40 LTA NLS (*green*, PDB:1EJL) at the same binding sites. (C) Interacting residues at the B19V NS1 cNLS major and minor binding sites of IMPα2ΔIBB. *Bold* represents hydrogen bonding and *italics* represents salt bridges.

Generally, cNLS binding to the IMPα major binding site is determined by the binding of cNLS amino acid side chains to IMPα amino acids within specific binding pockets (P), which are numbered from P0 to P6. In our structure, B19V NS1 K177 occupies the thermodynamically dominant P2 pocket at the major site, making an important hydrogen bond with G150, and both a salt bridge and hydrogen bond with D192 of IMPα2. The P3 and P5 pockets, which are known to make significant contributions to the binding energy (Hodel et al., 2001; Marfori et al., 2011), are occupied by B19V NLS1 residues K178 and R180, respectively. As expected, such positively charged residues are engaged in specific interactions with IMPα2 residues. In particular K178 is involved in two hydrogen bonds with N188 and one with N228 of IMPα2, whereas R180 engages with IMPα2 through two hydrogen bonds with N146, and one each with S105 and E181. The P4 pocket, which is the less important in determining the IMPα-NLS interaction, is occupied by B19V NS1 residue P179, which does not display any hydrogen bonds or salt bridges with IMPα2 in the crystal structure (Fig. 3AC). A comparison of viral NLS:IMPα2ΔIBB structures from the Protein Data Bank and a summary of the NLS residues interacting with the various IMPα binding pockets can be observed in Table 1. In most structures available, the P2 pocket is occupied by a K residue from monopartite cNLSs, with the exception of the atypical NLSs from Beak and Feather Disease Virus capsid (BFDV Cap), which presents an R, and from Epstein-Barr virus nuclear antigen LP (EBV NA LP) and MERS ORF4b, which both feature a V. Similarly, all NLSs accommodate either an R or a K in the P3 and P5 positions, whereas either basic (K, R) or hydrophobic (I, L, F, V, P) residues are found in the P4 pocket. Overall, our structure demonstrates a direct interaction between B19V NS1 and IMPα2ΔIBB, and suggests a critical role for the P2 residue K177.

3.3. B19V residue K177 is essential for direct binding to IMPα

To further validate the crystal structure of B19V NS1(172–182) and IMPα2ΔIBB, we investigated the effect of substitution of key basic residues with threonine. To this end, FITC-labelled peptides containing NS1 (172–182), NS1(172–182); K177T, or NS1(172–182); K178T sequences were subjected to native gel EMSA in the absence or presence of recombinantly purified mouse IMPα2ΔIBB. A FITC-labelled peptide corresponding to SV40-LTA NLS (P**KKKRK**V) was also used as a positive control for IMPα2ΔIBB binding (Fig. 4A). Our results indicated that >80% of NS1(172–182) peptide, but not of NS1(172–182); K177T and NS1(172–182); K178T peptides, co-migrated with IMPα2ΔIBB (Fig. 4BC). When FITC-peptides were incubated with increasing concentrations of IMPα2ΔIBB and binding measured in fluorescence polarization assays, NS1(172–182) peptide bound IMPα2ΔIBB with high affinity, with a Kd of c. 1 μM, while NS1(172–182); K178T peptide bound to a much lower extent, and NS1(172–182); K177T did not bind at all (Fig. 4DE), thus confirming the crucial role of NLS residues binding to the IMPα P2 pocket. Therefore, B19V NS1 NLS directly binds to IMPα, dependent on key basic residues.

3.4. B19V NS1 residues 172–182 confer nuclear targeting to heterologous proteins

We next decided to investigate the ability of NS1 residues 172–182 to target GFP to the cell nucleus. We quantitatively analyzed the nuclear accumulation of GFP fusion proteins transiently expressed in HEK293A cells by CLSM. Cells were transfected with expression plasmids encoding GFP alone or GFP fused to SV40-LTA NLS (P**KKKRK**V) as negative and positive controls, respectively, along with expression plasmids encoding GFP-NS1(172–182) and GFP-NS1(172–182); K177T (Fig. 5A). Our quantitative analysis revealed that GFP alone is evenly distributed between the nucleus and cytoplasm (Fig. 5B), with a Fn/c of c. 1 (Fig. 3C). On the other hand, GFP-SV40-LTA NLS strongly accumulated in the cell nucleus, with a Fn/c of ~8 (Fig. 5B). Importantly, GFP-NS1(172–182) similarly localized to the cell nucleus, with a Fn/c of ~6, while the subcellular localization of GFP-NS1(172–182); K177T was indistinguishable to that of GFP alone (Fig. 5BC). The observed nuclear targeting was determined to be due to IMPα/β active transport, as energy depletion as well as overexpression of the IMPα competitive inhibitor mcherry-Bimax2 (Tsujii et al., 2015), completely prevented nuclear accumulation of both GFP-SV40-LTA NLS and GFP-NS1(172–182). Bimax2 is a short, basic peptide, identified via systematic mutational analysis of a peptide template of a NLS as able to bind with extremely high affinity to IMPα isoforms in the absence of IMPβ, thereby specifically inhibiting the IMPα/β nuclear import pathway (Kosugi et al., 2008). Therefore, B19V NS1 residues 172–182 can confer nuclear targeting to GFP through an energy and IMPα/β-dependent pathway.

Table 1
Structurally characterized IMPα2ΔIBB/viral NLS complexes. The single letter amino acid code is used. B19V, Parvovirus B19; SV40, Simian vacuolating virus 40; LTA, large tumor antigen; NiV, Nipah virus; HeV, Hendra virus; HCMV, human cytomegalovirus; ZIKV, Zika virus; AAV, adeno-associated virus; EBV, Epstein-Barr virus; BFDB, beak and feather disease virus; DENV, dengue virus; MERS, middle-east respiratory syndrome; TBEV, tick borne encephalitis virus; HIV-1, human immunodeficiency virus type 1; VEEV, Venezuelan equine encephalitis virus.

Viral NLS	Residues Bound at Major Site Positions							Residues Bound at Minor Site Positions				PDB	REF
	P_0	P_1	P_2	P_3	P_4	P_5	P_6	$P_{1'}$	$P_{2'}$	$P_{3'}$	$P_{4'}$		
B19V NS1	H175	A176	K177	K178	P179	R180	I181	K177	K178	P179	R180	8F2Q	This work
SV40 LTA	P126	K127	K128	K129	R130	K131	V132	K128	K129	R130	K131	1EJL	Fontes et al. (2000)
Influenza PB2	A750	T751	K752	R753	I754	R755	M756	K738	R739	D740	S741	4UAF	Pumroy et al. (2015)
Influenza A NP	–	–	–	–	–	–	–	K7	R8	S9	Y10	4ZDU	Nakada et al. (2015)
NiV Virus W	P437	T438	K439	K440	A441	R442	V443	–	–	–	–	6BW0	Smith et al. (2018b)
HeV Virus W	P435	T436	K437	K438	A439	R440	V441	–	–	–	–	6BW1	Smith et al. (2018b)
HCMV pUL56	T821	R822	K823	R824	P825	R826	R827	K823	R824	P825	R826	5HUY	Sankhala et al. (2016)
HCMV pUL15	P183	K184	K185	R186	A187	K188	V189	K184	K185	R186	A187	5HUW	Sankhala et al. (2016)
ZIKV NS5	–	R389	K390	R391	P392	R393	V394	–	–	–	–	5W41	Ng et al. (2019)
AAV Po1 Cap	K150	K151	K152	K153	A154	R155	I156	–	–	–	–	7L04	Hoad et al. (2021)
EBV NA-LP	R44	R45	V46	R47	R48	R49	V50	–	–	–	–	5 × 8N	Nakada and Matsuura (2017)
EBV NA1	–	E378	K379	R380	P381	R382	S383	K379	R380	P381	R382	5WUN	Nakada et al. (2017)
BFDV Cap	Y18	R19	R20	R21	R22	R23	Y24	–	–	–	–	4HTV	Patterson et al. (2013)
DENV2 NS5	S885	M886	K887	R888	F889	R890	R891	–	–	–	–	5HHG	Tay et al. (2016)
DENV3 NS5	S885	M886	K887	R888	F889	R890	K891	–	–	–	–	5FC8	Tay et al. (2016)
MERS ORF4b	R33	Y34	V35	K36	R37	R38	F39	K23	R24	S25	H26	7RFX	Munasinghe et al. (2022)
HKU5 ORF4b	–	R31	K32	R33	R34	R35	H36	K32	R33	R34	R35	7RG6	Munasinghe et al. (2022)
TBEV Cap	–	Q89	K90	R91	G92	K93	R94	K76	I77	K78	R79	8ECH	
HIV-1 Tat	G48	R49	K50	K51	R52	R53	Q54	–	–	–	–	5SVZ	Smith et al. (2017)
HIV-1 Vpr	Q85	Q86	R87	R88	T89	R90	N91	R87	R88	T89	R90	5B56	Miyatake et al. (2016)
VEEV Cap	S62	A63	K64	K65	P66	K67	K68	–	–	–	–	3VE6	

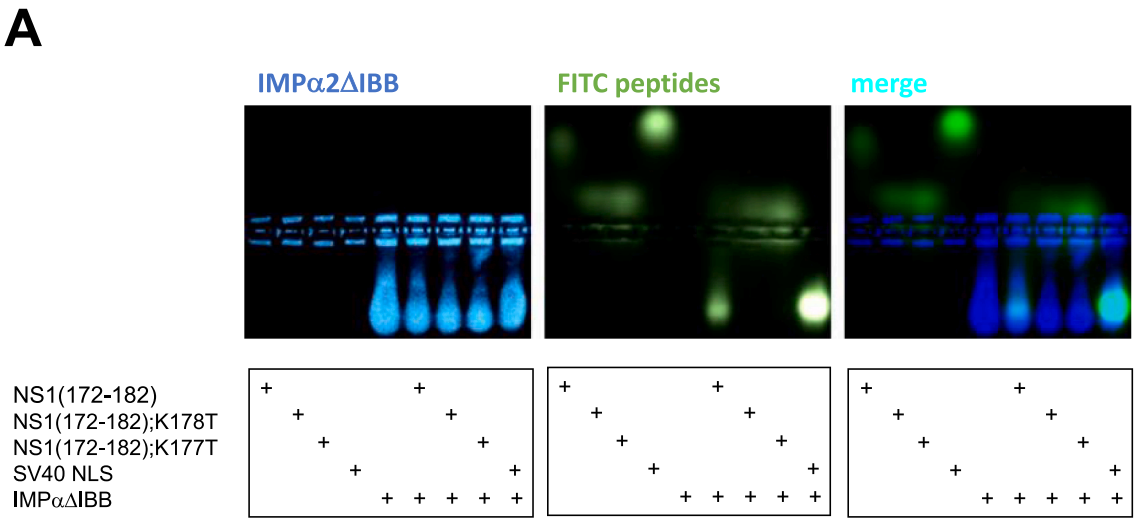

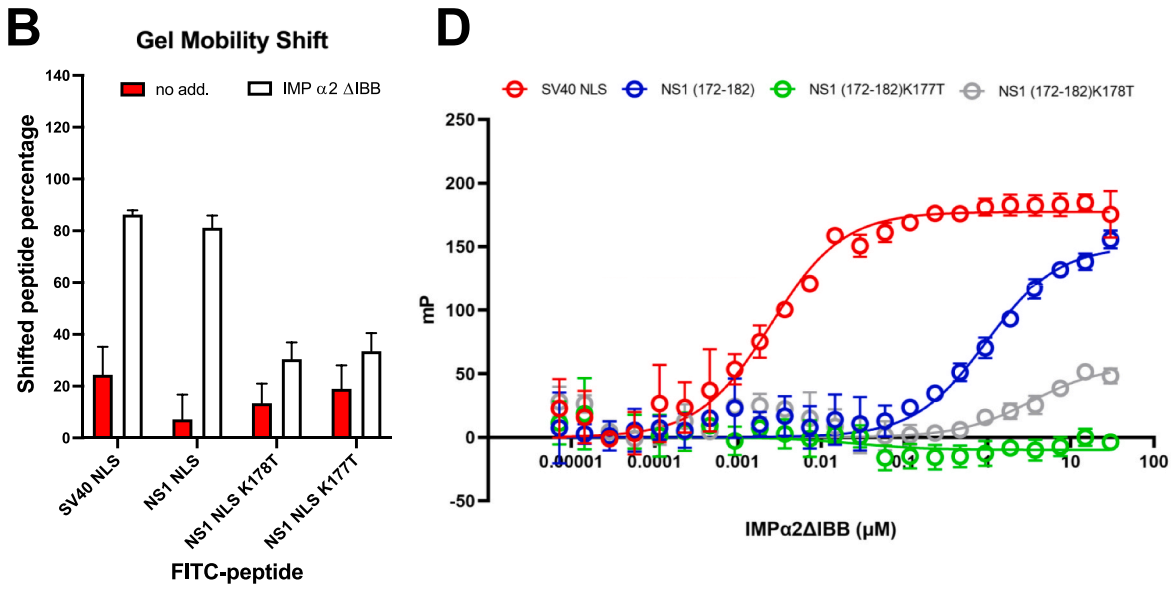

C

Shifted peptide (% of total)

	no add.			IMPα2ΔIBB		
	Mean	SEM	n	Mean	SEM	n
SV40 NLS	24.4	10.8	3	86.3	1.6	3
NS1 NLS	7.2	9.5	3	81.2	4.7	3
NS1 NLS K178T	13.4	7.6	3	30.4	6.5	3
NS1 NLS K177T	19.0	9.0	3	33.5	7.0	3

E

FP summary data

	Bmax		Kd (μM)	
	Value	SEM	Value	SEM
NS1 NLS	150.6	5.5	0.9	0.1
SV40 NLS	177.3	2.6	0.002	0.003

Fig. 4. B19V NS1 residues 172–182 directly interact with IMPα2ΔIBB with high affinity. (A) FITC-labelled peptides (10 μM) and bacterially purified recombinant IMPα2ΔIBB protein (20 μM) were incubated as indicated (*bottom panel*), prior to being subjected to an EMSA, as described in the Materials and Methods. Coomassie staining of the gel is shown in *blue* (*left panel*; IMPα2ΔIBB), a fluorescent image after excitation at 488 nm is shown in *green* (*middle panel*; FITC-peptides), and a merged image of the two channels is shown in *cyan* (*right panel*; merge). (B) The percentage of shifted peptides that were (*blue bars*) or were not (*red bars*) incubated with IMPα2ΔIBB is shown as mean ± standard error of the mean (SEM) relative to three independent experiments, along with the results from two-way ANOVA with a Fisher's Least Significant Difference (LSD) post hoc test. ****: $p < 0.0001$. (C) Summary table relative to data shown in (B). (D) FITC-labelled peptides (10 nM) were incubated with two-fold serial dilutions of bacterially purified recombinant IMPα2ΔIBB (range: 30 μM to $7.15x10^{-3}$ nM) and subjected to fluorescence polarization analysis. Data are shown in millipolarized units (mP) as mean ± SEM relative to three independent experiments. Data were analyzed with GraphPad Prism using the one site specific binding least squares fit function to calculate the Bmax and Kd relative to the peptide- IMPα2ΔIBB interaction. (E) Summary table relative to data shown in (D), with mean Bmax and Kd values relative to the interaction of indicated peptides with IMPα2ΔIBB, along with the respective SEM.

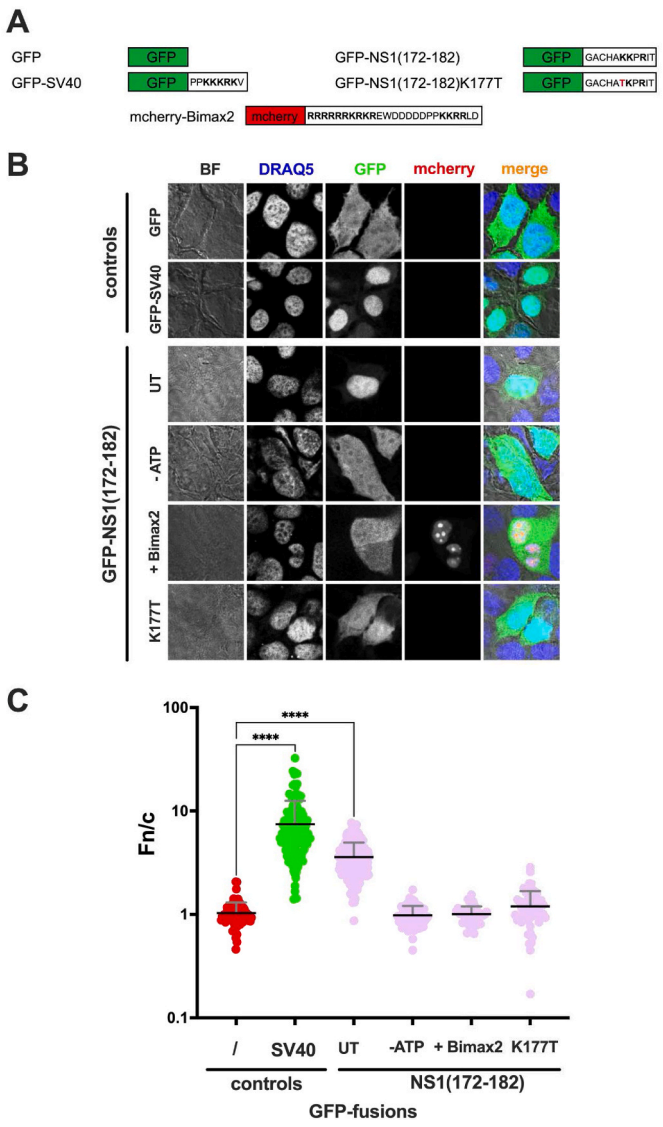

Fig. 5. B19V NS1 residues 172–182 represent a functional monopartite cNLS. (A) HEK293A cells were transfected with appropriate plasmids to transiently express the indicated GFP fusion proteins. (B) 48 h post transfection, cells were treated with DRAQ5 to stain cell nuclei, processed and mounted on slide holders for CLSM analysis. Representative images of the bright field (BF), the cell nuclei (DRAQ5) and expressed fusion proteins (GFP, mcherry) are shown, along with a merged image of the three channels (merge). (C) Micrographs such as those shown in (B) were quantitatively analyzed to calculate the levels of nuclear accumulation (Fn/c) relative to the indicated fusion proteins at the single cell level, as described in the Materials and Methods. Data shown are individual measurements along means +SD of the mean relative to pooled data from at least 100 cells and two independent experiments. Results from Brown-Forsythe and Welch ANOVA tests among cells expressing the indicated GFP fusions and GFP alone are reported on top. ****: $p < 0.0001$.

3.5. B19V NS1 is translocated into the nucleus via the IMPα/β heterodimer

Our data strongly support the idea of B19V NS1 being translocated into the nucleus by IMPα/β through the monopartite cNLS localized at residues 172–182. To further investigate this, we quantitatively analyzed the subcellular localization of transiently expressed GFP-NS1 in the absence and presence of mcherry-Bimax2 (Tsujii et al., 2015). GFP-H1E, which is imported into the nucleus in an IMPα/β independent fashion (Jakel et al., 1999), and GFP-HCMV-UL44, which is imported into the nucleus by IMPα/β (Alvisi et al., 2005), were also expressed as negative and positive controls, respectively (Fig. 6A). As expected, all GFP-fusions strongly accumulated in the cell nucleus in the absence of mcherry-Bimax2 (Fig. 6B), with Fn/c ranging from ~500 for GFP-H1E to ~10 for GFP-NS1 (Fig. 6C), and a Fn/c > 2 in 100% of analyzed cells (Fig. 6D). Also as expected, co-expression with mcherry-Bimax2 did not significantly affect nuclear accumulation of GFP-H1E (Fn/c of ~500), but completely abolished that of GFP-HCMV-UL44 (Fn/c of ~50 to 0.1). Importantly, in the presence of mcherry-Bimax2, GFP-NS1 failed to accumulate in the cell nucleus (Fn/c of 0.2, Fig. 6C), in 100% of analyzed cells (Fig. 6D). The K177T substitution, similarly impaired nuclear import (Fig. 6CD). Our results clearly indicate that B19V NS1 is transported into the nucleus via IMPα/β, through binding of IMPα to its monopartite cNLS located at residues 172–182.

3.6. Inhibition of IMPα/β interferes with B19V DNA replication

Since the B19V genome is replicated in the nucleus of infected cells via a complex process which involves the activity of NS1, we reasoned that inhibition of NS1 nuclear import could result in inhibition of viral genome replication. We therefore tested the effect on B19V replication of pharmacological inhibition of IMPα/β on B19V replication, as mediated by the FDA approved anti parasitic drug IVM. UT7/Epo-S1 cells, either untreated or treated for 6 h in the presence of different concentrations of IVM, were infected with B19V for 2h in the absence of IVM. After 2 washes in PBS to remove residual viral particles, cells were further incubated for a time course of infection either untreated or treated with IVM as in the previous condition. Viral transcription and DNA replication were evaluated at 2h and 48h post infection. In parallel, cells were either incubated with increasing concentrations of IVM or left untreated, and cell viability was measured (Fig. 7A). Our data indicated that IVM was well tolerated up to 10 μM (Fig. 7D). At such dosage, IVM treatment showed very little effect on B19V transcription, causing a 20% inhibition at 48h post infection (Fig. 7B), whereas a more pronounced effect on B19V DNA replication was observed, with inhibition of ~80% as compared to untreated cells (Fig. 7C). Intriguingly, treatment with 10 μM IVM did not affect the total number of cells at 48h post infection (Fig. 7E), but significantly decreased the number of detectable B19V NS1 positive cells (Fig. 7F). Consistent with the idea that such IVM-mediated impairment in B19V DNA replication is the consequence of reduced nuclear import of NS1, IVM significantly reduced the level of NS1 nuclear accumulation at 24 h post infection (Fn/c from 2.4 to 1.7, Fig. 7G).

3.7. NS1 nuclear import is essential for B19V genome replication

The remarkable reduction of B19V DNA replication upon treatment with IVM suggested a crucial role for NS1 nuclear import during the B19V life cycle. However, such inhibition could also result from the pleiotropic properties of IVM rather than its effect on nuclear import, or the inhibition of nuclear transport of cellular factors essential for viral replication. To directly investigate the role of NS1 nuclear import in the B19V life cycle, we tested the effect of the K177T substitution, preventing NS1 nuclear import, on genome expression and replication. For this purpose, we utilized a mini genome self-amplification B19V replicon that we recently described (Reggiani et al., 2022). To this end, UT7/Epo-S1 cells were nucleofected with PCR products containing CH10 pAs1, a minigenome whose coding potential is restricted to the NS1 protein (Fig. 8A), either wt or its substitution derivative K177T impaired in nuclear import. As a further control, a CH10 pAs1 minigenome whereby the start codon of full length NS1 was mutagenized to prevent expression (NS1 ATG-KO) was also transfected. NS1 expression and its subcellular localization were assessed by CLSM (Fig. 8BC). As expected, NS1 could be detected in UT7/Epo-S1 cells transfected with NS1 wt and K177T NS1 starting from 24 h post transfection, while no NS1 could be detected in cells transfected with the NS1 ATG-KO pCH10-pAs1 minigenome, confirming that, in the absence of the

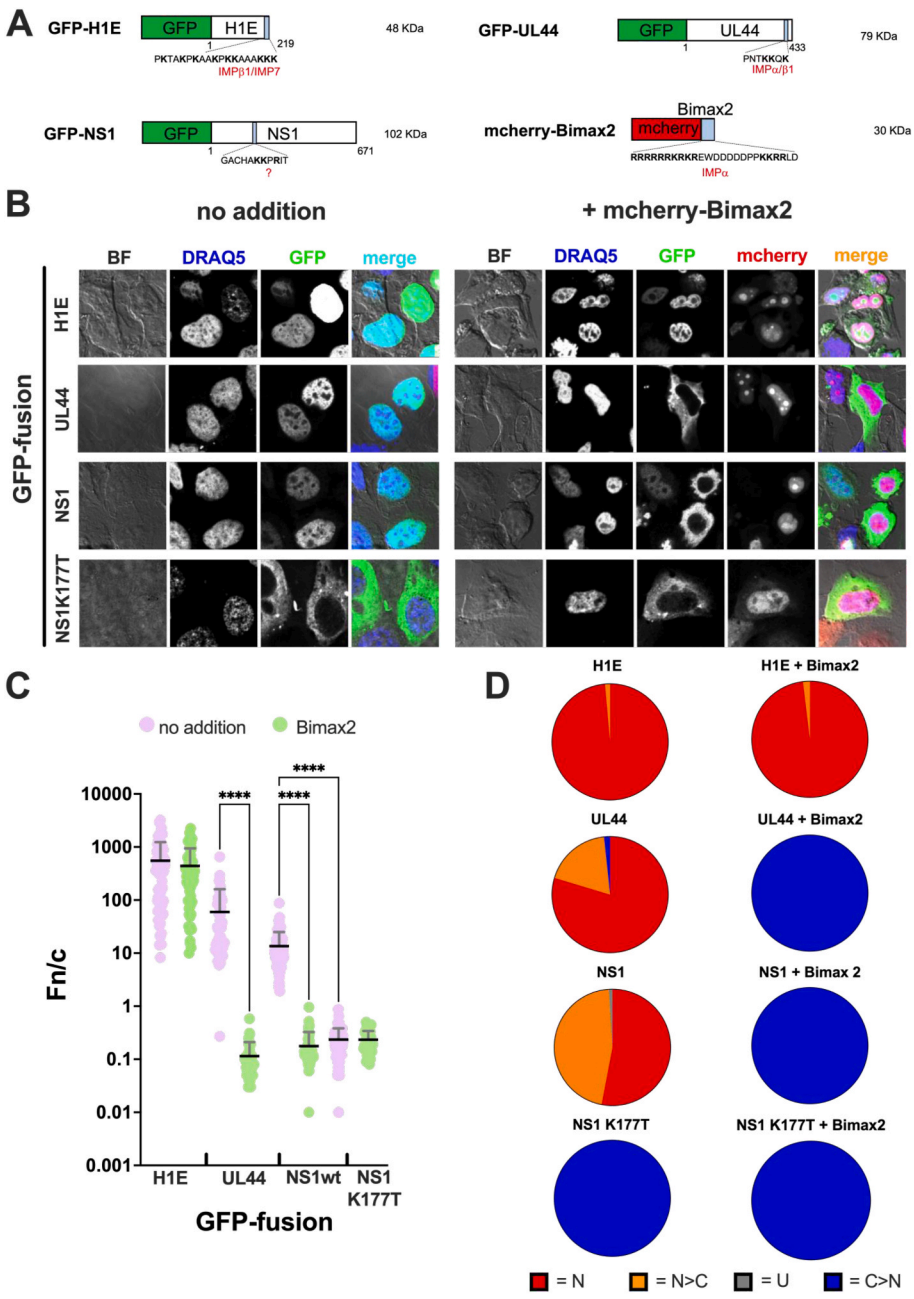

Fig. 6. B19V NS1 is translocated into the host cell nucleus via the IMPα/β **heterodimer.** (A) HEK293A cells were transfected with appropriate mammalian expression plasmids to transiently express the indicated fusion proteins. (B) 48 h post transfection, cells were treated with DRAQ5 to stain cell nuclei, processed and mounted on slide holders for CLSM analysis. Representative images of the brightfield (BF), cell nuclei (DRAQ5), expressed fusion proteins (GFP) and mcherry-Bimax2 (mcherry) are shown, along with a merged image of the four channels (merge), for cells expressing the indicated fusion proteins, expressed either in the absence (no addition) or presence (+mcherry-Bimax2) of mcherry-Bimax2. (C) Micrographs such as those shown in (B) were quantitatively analyzed to calculate the levels of nuclear accumulation (Fn/c) relative to the indicated fusion proteins at the single cell level, as described in the Materials and Methods. Data shown are individual measurements and means ± SD of the mean relative to pooled data from at least 100 cells and two independent experiments. Results from Brown-Forsythe and Welch ANOVA tests among cells expressing the indicated GFP fusions alone and in the presence of mcherry-Bimax2 are reported on top. ****: $p \leq 0.0001$. (D) The subcellular localization of the indicated GFP fusion protein at the single cell level was classified as nuclear (N: Fn/c > 10), more nuclear than cytosolic (N > C: 2 < Fn/c < 10), ubiquitous (U: 1 < Fn/c < 2), or more cytosolic than nuclear (C > N: Fn/c < 1). The percentage of cells with the indicated phenotypes is shown.

upstream ATG, NS1 was not expressed at detectable levels (Fig. 8BC). Importantly, while NS1 wt could translocate to the cell nucleus (Fn/c = 1.5 ± 0.9), the K177T substitution caused strong mislocalization to the cytosol (Fn/c = 0.2 ± 0.2). Accordingly, sustained viral transcription could be measured at both 24h and 48h post transfection upon transfection with NS1wt (Fig. 8DE, *left panels*) but not with NS1 ATG-KO (Fig. 8DE, *right panels*). Importantly, gene expression post transfection with NS1 K177T was also reduced, albeit to a lesser extent as compared to NS1 ATG-KO (Fig. 8DE, *middle panels*). Overall, such results highlight the importance of NS1 nuclear transport in B19V genome expression and replication.

4. Discussion

B19V is a major human pathogen causing severe diseases in immunocompromised individuals and in cases of vertical transmission (Bonvicini et al., 2017a; Brown, 2000). Here we have begun the characterization of B19V NS1 nuclear import (Figs. 2–6) and shown its importance for B19V replication (Figs. 7–8).

4.1. B19V NS1 contains a monopartite cNLS

NS1 nuclear import is dependent on a cNLS located within residues 172–182, which we showed is able to both bind IMPα2ΔIBB with high affinity (Fig. 4) and confer energy and IMPα/β−dependent nuclear targeting to heterologous proteins (Fig. 5). Such properties are typical of bona fide cNLSs (Alvisi et al., 2005, 2006b, 2007, 2008). To obtain structural insights regarding the B10V NS1-IMPα interaction, we solved the crystal structure of NS1 residues (172–182) in complex with mouse IMPα2ΔIBB (Fig. 3). Mouse IMPα2 is an orthologue of human IMPα1, with which it shares 99% amino acid similarity, and is the most commonly used IMPα for crystallographic analyses (see Table 1 and references therein). In our structure, B19V NS1(172–182) was bound at both the major and minor sites of IMPα2. However, the latter interaction

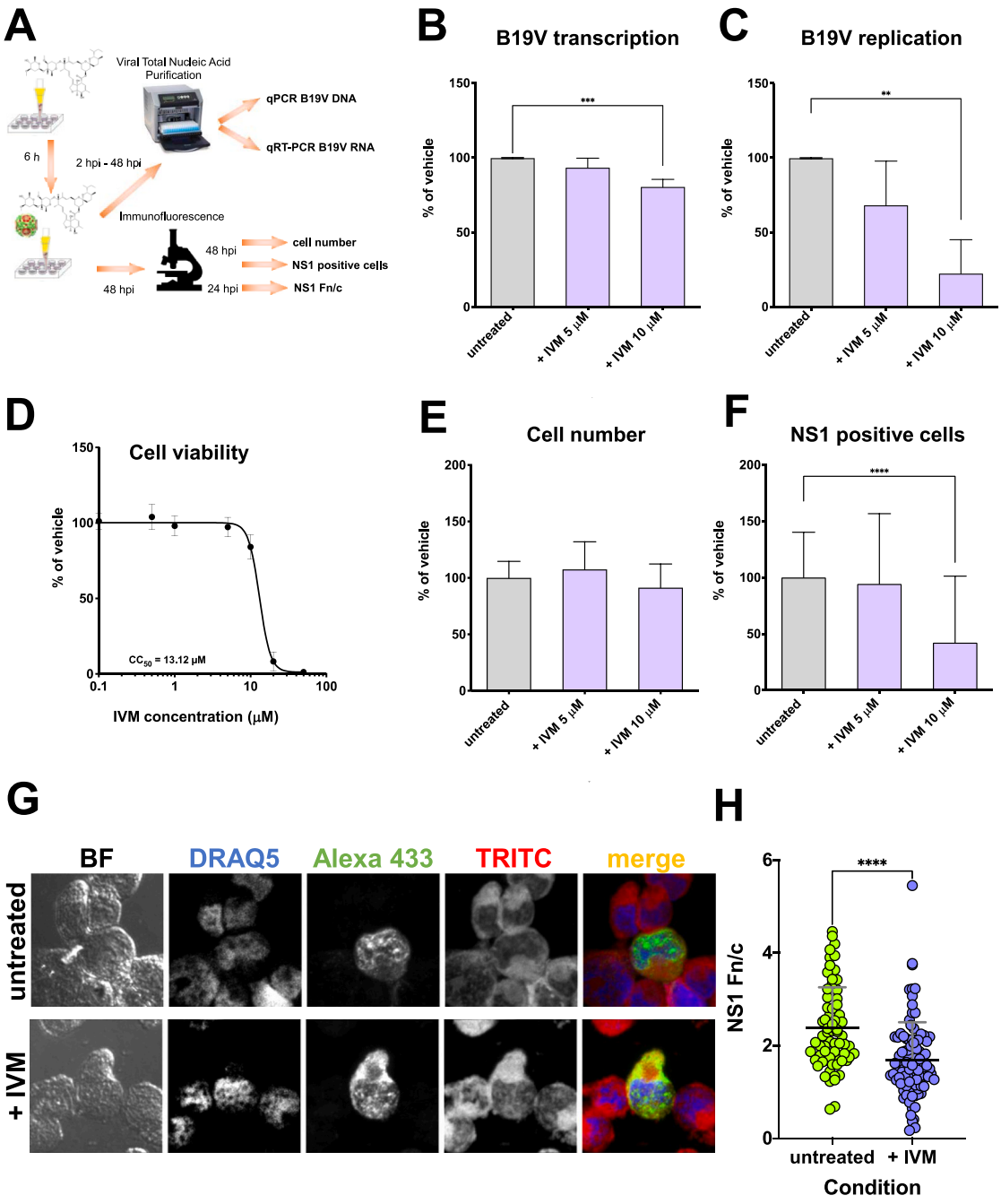

Fig. 7. Pharmacological inhibition of the IMPα/β **nuclear import pathway impairs B19V replication.** (A). Schematic representation of the experimental set up. (B, C) Quantification of viral nucleic acids in UT7/Epo-S1 cells. Cells were pre-treated for 6 h with 0, 5, or 10 μM IVM, before being infected with B19V. Infected cells were left untreated or further incubated with 5 or 10 μM IVM for 48 h. Results for quantification of B19V total RNA (B) and viral DNA (C) are expressed as percentage values compared to untreated cells. Data are shown as mean ± SD of the mean relative to three independent experiments, along with results from Brown-Forsythe and Welch ANOVA tests with Dunnett T3 multiple comparison. ** = $p < 0.01$; *** = $p < 0.001$. (D) Normalized dose-response curve, calculated from CCK8 assay data obtained at 48 h post treatment of uninfected UT7/Epo-S1 cells. Cell viability as a function of IVM concentration, was expressed as mean percentage value compared to control samples. (E, F) Effect of IVM on cell number and NS1 expression. Cells were pretreated for 6 h with 0, 5 or 10 μM IVM, before being infected with B19V. Infected cells were left untreated or further incubated with 5 or 10 μM IVM. At 48 h post infection, cells were harvested and processed as described in the Materials and Methods to enable microscopic detection of cell nuclei by staining with DRAQ5, NS1 by incubation with a monoclonal antibody followed by incubation with a secondary antibody conjugated to AlexaFluor 488, and actin filaments by staining with TRITC-phalloidin. Samples were then analyzed with a Leica epi-fluorescence microscope equipped with a 20× objective to count the number of cells (E), and the number NS1 positive cells per each field (F). Data were normalized to untreated cells, and are expressed as means ± SD, relative to three independent experiments along with results from Brown-Forsythe and Welch ANOVA tests with Dunnett T3 multiple comparison. ****: $p < 0.0001$. (G) At 24 h post infection, cells were similarly processed for quantitative CLSM with a Nikon A1 confocal laser microscope equipped with a 60× oil immersion objective. Representative images of the brightfield (BF), cell nuclei (DRAQ5), NS1 (Alexa 488) and actin filaments (TRITC) relative to randomly chosen fields are shown, along with merged images in the *right panels*. (H) Micrographs such as those shown in (G) were quantitatively analyzed to calculate the level of nuclear accumulation of NS1 (Fn/c) at the single cell level. Data shown are single measurements and means ± SD relative to pooled data ($n > 60$) from three independent experiments, along with results from the Welch's *t*-test. **: $p < 0.005$.

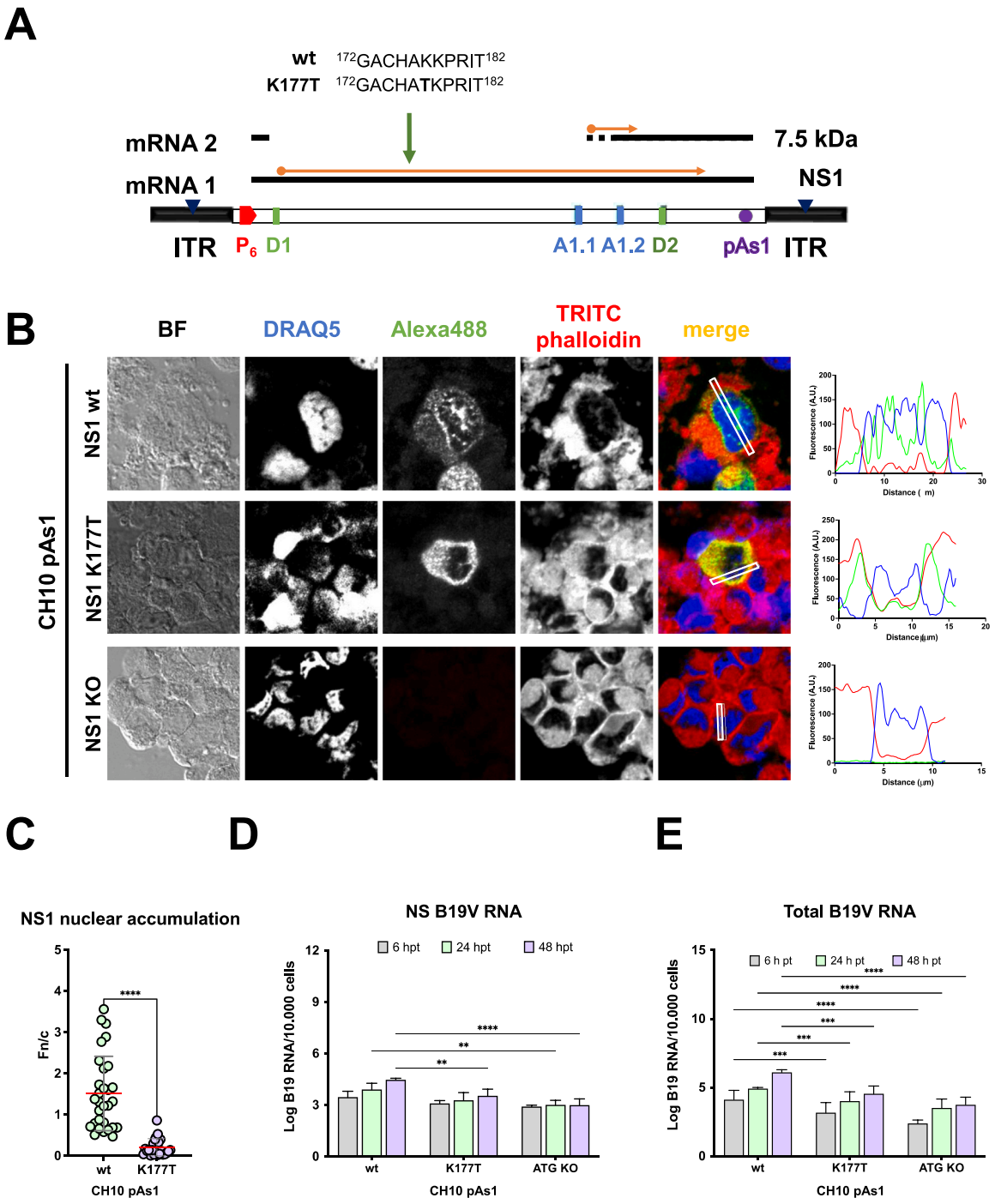

Fig. 8. Nuclear transport of NS1 is required for viral B19V gene expression and replication in a minigenome system. (A) Schematic diagram of B19V CH10 pAs1 minigenomes. ITR, inverted terminal regions; IR, internal region; cis-acting functional sites: P6, promoter; pAs1, engineered cleavage-polyadenylation sites; D1, D2, splice donor sites; A1.1, A1.2, splice acceptor sites. Top: Open reading frames and coding sequences for the viral proteins. NS, non-structural protein NS1; 7.5 kDa, putative minor non-structural protein. UT7/Epo-S1 cells were nucleofected with PCR products encompassing the CH10 pAs1 B19V minigenome containing either wt, ATG KO or K177T NS1 sequences as described in the Material and Methods. At 6 h, 24 h and 48 h post transfection cells were harvested and either processed for immunofluorescence analysis to calculate the levels of nuclear accumulation of NS1, or for RT-PCR detection of viral transcripts (D, E). (B) Confocal images of cells nucleofected with the indicated PCR-derived minigenomes. Representative images of the cell nuclei (DRAQ5), NS1 (Alexa 488) and actin filaments (TRITC phalloidin) channels are shown, along with a merged image of the three channels (merge). (C) Micrographs such as those shown in (B) were quantitatively analyzed to calculate the Fn/c ratio at the single cell level. Data shown are single measurements of single cells from three independent experiments, along with mean and SD of the mean. ****: $p \leq 0.0001$ according to student's *t*-test with Welch's correction. (D, E) Results for quantification of NS1 (D) and total (E) B19V transcripts depicted in (A) are shown as mean ± SD of the mean relative to three independent experiments. **: $p \leq 0.01$; ***: $p \leq 0.001$; ****: $p \leq 0.0001$ following two-way ANOVA and Tukey post hoc tests.

is most likely an artifact due to the high concentration of peptide required for crystallization, similarly to what has been observed for other monopartite cNLSs, such as the SV40 LTA NLS bound to mouse and yeast IMPαs (Conti et al., 1998; Fontes et al., 2000), as well as other IMPα-NLS structures (Nakada et al., 2017; Nakada and Matsuura 2017; Sankhala et al., 2016; see also Table 1). B19V NS1 K177 occupies the thermodynamically dominant P2 pocket in the IMPα2 major site (Hodel et al., 2001), and is accordingly the only NS1 residue forming a salt bridge with IMPα2. The IMPα2 P3 and P5 positions are occupied by B19V NS1 K178 and R180, respectively, with such positively charged residues are known to make significant contributions to the binding energy (Hodel et al., 2001; Marfori et al., 2011). The IMPα2 P4 pocket is occupied by B19V NS1 P179, and although this is an interfacing residue, it does not display any hydrogen bond or salt bridges with IMPα2 in the crystal structure (Fig. 3AC). This binding pocket contributes less to the cNLS binding strength and can accommodate a wide range of amino acid side chains, including hydrophobic ones such as in V, M, A and P, although with lower affinity than K and R (see Table 1). As such, the heterogeneous P4 pocket has been proposed to play a role in modulating cNLS function (Smith et al., 2018a). The presence of a P residue in the P4 pocket can therefore explain, at least in part, the lower activity of the B19V NS1 cNLS when fused to GFP (Fig. 5) and its lower binding affinity to IMPα2ΔIBB in FP assays (Fig. 4) when compared to SV40 LTA cNLS, which has a R residue in the corresponding P4 pocket (Fig. 3B).

4.2. Effect of the K177T substitution on B19V NS1-IMPα binding and nuclear translocation

Substitution of the B19V NS1 cNLS P2-interacting residue K177 to a T abrogated the ability of a FITC-labelled peptide to bind to IMPα2ΔIBB (Fig. 4), and abolished NLS activity when fused to GFP (Fig. 5).A K to T substitution involving the K127 residue of the SV40 LTA cNLS which similarly occupies the P2 pocket of IMPα2 (Fig. 3B), was originally described as being capable of completely abrogating IMPα2 binding and nuclear import (Conti et al., 1998; Hodel et al., 2001; Lanford and Butel, 1984). The cNLS characterized here appears to be the main determinant of NS1 nuclear targeting, since impairment of NS1 nuclear transport was observed after transient expression of a GFP-NS1; K177T fusion protein in HEK293-A cells (Fig. 6), as well as upon nucleofection of UT7/EpoS1 cells with the B19V CH10 pAs; NS1K177T minigenome (Fig. 8). This fully supports the idea that during B19V infection, NS1 nuclear import is mediated by the cNLS identified here, similarly to what has been reported for NS1 from MVM and PPV, whose NLSs are essential for nuclear import (Cao et al., 2022; Ihalainen et al., 2007).

4.3. The cNLS from B19V NS1 is not conserved in other Parvoviridae members

This is the third different NLS reported on NS1 from *Parvoviridae* members. While those identified from MVM and PPV are bipartite in nature, the one characterized here is monopartite (Figs. 1B and 3A). Therefore, although the use of cNLSs appears to be conserved across different parvoviruses, their evolution is likely quite diverse (Fig. 1BC). Such heterogenicity in terms of NLS architecture is not uncommon among orthologues belonging to the same viral family. For example, while viral DNA polymerase subunits encoded by Human Herpes Virus type 1, pUL30 and pUL42, are bipartite cNLSs (Alvisi et al., 2007, 2008), those encoded by HCMV, pUL54 and ppUL44 are monopartite (Alvisi et al., 2005, 2006b). It is not clear the reason why B19V evolved a monopartite cNLS on NS1 whereas MVM and PPV evolved bipartite ones. Since it has been widely reported that bipartite cNLSs bind IMPα with higher affinity than monopartite cNLSs (Hoad et al., 2023), it is possible that B19V NS1 evolved to possess a weak cNLS, thus avoiding excessive nuclear accumulation of NS1 during infection. This hypothesis is also in accordance with the presence of a B19V NS1 cNLS P residue in the P4 pocket of the IMPα2 major binding site (see above, and Fig. 3).

4.4. Correlation between B19V NS1 localization and function

While we clearly showed that B19V NS1 accumulates in the host cell nucleus (Fn/c c. 3) from 16 h post infection (Fig. 2), NS1 could also be detected in the cytosol, consistent with previous reports (Luo et al., 2013; Zeng et al., 2022). This is not surprising, since NS1 has been shown to interact with several proteins endowed with cytosolic localization, such as Cyclin B (Pines and Hunter, 1994). Furthermore, NS1 K177C, which is defective for nuclear localization, retained the ability to induce apoptosis upon transduction of EPCs (Wan et al., 2010). Taken together, these findings imply possible functional roles of NS1 in the cytoplasm (Zeng et al., 2022). Regardless, NS1 nuclear localization is consistent with several key functions of B19V NS1 during viral infection, including its role in binding to the viral origin of replication and nicking the viral genome (Sanchez et al., 2016), as well as its ability to act as a viral and cellular transactivator (Luo et al., 2013; Moffatt et al., 1998; Morita et al., 2003; Raab et al., 2002), and to facilitate nuclear import of transcription factors E24 and E2F5, thus causing cell cycle arrest and promoting viral replication (Wan et al., 2010).

4.5. Nuclear transport pathway of B19V NS1

Several lines of evidence argue that B19V NS1 is imported into the nucleus by the IMPα/β heterodimer. Firstly, as alluded to above, its cNLS can complex with IMPα2 (Figs. 3 and 4). Secondly, the K177T substitution, which abrogates IMPα2 binding (Fig. 4), also abrogated nuclear localization of NS1 (Figs. 6 and 8). Thirdly, co-expression with Bimax2, a peptide capable of binding to IMPα with very high affinity in the absence of IMPβ, thereby selectively inhibiting the IMPα/β but no other nuclear import pathways (Gonzalez et al., 2021; Kosugi et al., 2008; Li et al., 2013; Li et al., 2021; Tsujii et al., 2015), strongly reduces GFP-NS1 nuclear import in HEK293A cells (Fn/c decreases from 13.6 to 0.2; Fig. 6). Importantly, expression of Bimax2 also inhibited nuclear import of a HCMV UL44, which has been extensively characterized as an IMPα/β cargo (Alvisi et al., 2005, 2011), but not of H1E, which can be transported into the nucleus by IMP7 (Jakel et al., 1999). Lastly, treatment of cells with the FDA approved antiparasitic drug IVM, which has been shown to specifically inhibit the IMPα/β pathway (Wagstaff et al., 2011; Yang et al., 2020), significantly reduced NS1 nuclear import in UT7/Epo-S1 cells (Fn/c decreases from 2.4 to 1.7; Fig. 7GH).

4.6. B19V NS1 nuclear import as an antiviral strategy

Significantly, hindering NS1 nuclear import, either by treating cells with IVM, or introducing the K177T substitution, had dramatic effects on viral replication, both in infected cells (Fig. 7), and in a minigenome context, whereby the structural proteins VP1 and VP2 are not expressed (Fig. 8), respectively. Our results have pharmacological implications for the development of antivirals to combat B19V infection. the IMPα/β specific inhibitor IVM (Wagstaff et al., 2011), has been reported to successfully inhibit replication of a number of viruses, including PPV (Barrows et al., 2016; Caly et al., 2020; Cao et al., 2022; Ketkar et al., 2019; Lv et al., 2018; Mastrangelo et al., 2012; Raza et al., 2020; Tay et al., 2013; Wagstaff et al., 2012; Wang et al., 2019; Xu et al., 2018; Yang et al., 2019). IVM-mediated inhibition of IMPα/β-dependent nuclear import in B19V infected UT7/Epo-S1 cells significantly reduced viral replication (Figs. 7D and 80% inhibition). Such evidence, taken together with the absence of a cNLS in the capsid protein VP1 (Deng et al., 2013), which is believed to be responsible for nuclear import of viral genomes (Fig. 1), suggests that the observed reduction in viral replication is due to inhibition of NS1 nuclear import rather than genome uncoating. This idea is further strengthened by the marked reduction in viral genome transcription observed upon transfection of UT7/Epo-S1 cells with a pCH10 pAs1 minigenome mediating the expression of a NS1 K177T substitution derivative compared to NS1wt (Fig. 8). B19V pCH10 pAs1 minigenomes are capable of self-amplifying

but lack the coding information for B19V structural proteins, and therefore represent an ideal tool for dissecting the role of individual substitutions in NS1 (Reggiani et al., 2022). Overall, our results support NS1 nuclear targeting as a potential tool for antiviral intervention. Since IVM has been reported to have pleiotropic effects besides inhibition of the IMPα/β nuclear transport pathway, ranging from binding to glutamate-gated chloride channels to inhibition of viral helicases (Mastrangelo et al., 2012) it is unlikely that the concentrations needed for antiviral activity would be tolerable in patients. This precludes its use as an antiviral compound in the clinic, as shown for other viruses, including SARS-CoV-2, despite efficient virus suppression *in vitro* (Ketkar et al., 2019; Reis et al., 2022). In this context, the crystallographic structure of B19V NS1 cNLS in complex with IMPα2ΔIBB reported here will prove invaluable towards the identification of more specific inhibitors of B19V replication acting on NS1 nuclear import, which will be the object of future work in our laboratories.

Declaration of competing interest

The authors declare that they have no known competing financial interests or personal relationships that could have appeared to influence the work reported in this paper.

Data availability

Data will be made available on request.

Acknowledgements

This work was partially supported by University of Padua (BIRD grant ALVI_SID19_01 and DOR grants to G.A) and Italian Ministry of University and Research (grant PRIN 2017 9JHAMZ_007 to G.G). This research was undertaken in part using the MX2 beamline at the Australian Synchrotron, part of ANSTO, and made use of the Australian Cancer Research Foundation (ACRF) detector.

Appendix A. Supplementary data

Supplementary data to this article can be found online at https://doi.org/10.1016/j.antiviral.2023.105588.

References

Adams, P.D., Afonine, P.V., Bunkoczi, G., Chen, V.B., Davis, I.W., Echols, N., Headd, J.J., Hung, L.W., Kapral, G.J., Grosse-Kunstleve, R.W., McCoy, A.J., Moriarty, N.W., Oeffner, R., Read, R.J., Richardson, D.C., Richardson, J.S., Terwilliger, T.C., Zwart, P.H., 2010. PHENIX: a comprehensive Python-based system for macromolecular structure solution. Acta Crystallogr., Sect. D: Biol. Crystallogr. 66, 213–221.

Alvisi, G., Jans, D., Guo, J., Pinna, L., Ripalti, A., 2005. A protein kinase CK2 site flanking the nuclear targeting signal enhances nuclear transport of human cytomegalovirus ppUL44. Traffic 6, 1002–1013.

Alvisi, G., Jans, D., Ripalti, A., 2006a. Human cytomegalovirus (HCMV) DNA polymerase processivity factor ppUL44 dimerizes in the cytosol before translocation to the nucleus. Biochemistry 45, 6866–6872.

Alvisi, G., Ripalti, A., Ngankeu, A., Giannandrea, M., Caraffi, S.G., Dias, M.M., Jans, D.A., 2006b. Human cytomegalovirus DNA polymerase catalytic subunit pUL54 possesses independently acting nuclear localization and ppUL44 binding motifs. Traffic 7, 1322–1332.

Alvisi, G., Musiani, D., Jans, D.A., Ripalti, A., 2007. An importin alpha/beta-recognized bipartite nuclear localization signal mediates targeting of the human herpes simplex virus type 1 DNA polymerase catalytic subunit pUL30 to the nucleus. Biochemistry 46, 9155–9163.

Alvisi, G., Avanzi, S., Musiani, D., Camozzi, D., Leoni, V., Ly-Huynh, J.D., Ripalti, A., 2008. Nuclear import of HSV-1 DNA polymerase processivity factor UL42 is mediated by a C-terminally located bipartite nuclear localization signal. Biochemistry 47, 13764–13777.

Alvisi, G., Marin, O., Pari, G., Mancini, M., Avanzi, S., Loregian, A., Jans, D.A., Ripalti, A., 2011. Multiple phosphorylation sites at the C-terminus regulate nuclear import of HCMV DNA polymerase processivity factor ppUL44. Virology 417, 259–267.

Alvisi, G., Jans, D.A., Camozzi, D., Avanzi, S., Loregian, A., Ripalti, A., Palu, G., 2013. Regulated transport into the nucleus of herpesviridae DNA replication core proteins. Viruses 5, 2210–2234.

Alvisi, G., Paolini, L., Contarini, A., Zambarda, C., Di Antonio, V., Colosini, A., Mercandelli, N., Timmoneri, M., Palu, G., Caimi, L., Ricotta, D., Radeghieri, A., 2018. Intersectin goes nuclear: secret life of an endocytic protein. Biochem. J. 475, 1455–1472.

Aragao, D., Aishima, J., Cherukuvada, H., Clarken, R., Clift, M., Cowieson, N.P., Ericsson, D.J., Gee, C.L., Macedo, S., Mudie, N., Panjikar, S., Price, J.R., Riboldi-Tunnicliffe, A., Rostan, R., Williamson, R., Caradoc-Davies, T.T., 2018. MX2: a high-flux undulator microfocus beamline serving both the chemical and macromolecular crystallography communities at the Australian Synchrotron. J. Synchrotron Radiat. 25, 885–891.

Barrows, N.J., Campos, R.K., Powell, S.T., Prasanth, K.R., Schott-Lerner, G., Soto-Acosta, R., Galarza-Munoz, G., McGrath, E.L., Urrabaz-Garza, R., Gao, J., Wu, P., Menon, R., Saade, G., Fernandez-Salas, I., Rossi, S.L., Vasilakis, N., Routh, A., Bradrick, S.S., Garcia-Blanco, M.A., 2016. A screen of FDA-approved drugs for inhibitors of Zika virus infection. Cell Host Microbe 20, 259–270.

Berns, K.I., 1990. Parvovirus replication. Microbiol. Rev. 54, 316–329.

Bonvicini, F., Filippone, C., Manaresi, E., Zerbini, M., Musiani, M., Gallinella, G., 2008. Functional analysis and quantitative determination of the expression profile of human parvovirus B19. Virology 381, 168–177.

Bonvicini, F., Bua, G., Gallinella, G., 2017a. Parvovirus B19 infection in pregnancy-awareness and opportunities. Curr. Opin. Virol. 27, 8–14.

Bonvicini, F., Bua, G., Conti, I., Manaresi, E., Gallinella, G., 2017b. Hydroxyurea inhibits parvovirus B19 replication in erythroid progenitor cells. Biochem. Pharmacol. 136, 32–39.

Brown, K.E., 2000. Haematological consequences of parvovirus B19 infection. Baillieres Best Pract Res Clin Haematol 13, 245–259.

Bua, G., Manaresi, E., Bonvicini, F., Gallinella, G., 2016. Parvovirus B19 replication and expression in differentiating erythroid progenitor cells. PLoS One 11, e0148547.

Caly, L., Druce, J.D., Catton, M.G., Jans, D.A., Wagstaff, K.M., 2020. The FDA-approved drug ivermectin inhibits the replication of SARS-CoV-2 in vitro. Antivir. Res. 178, 104787.

Cao, L., Fu, F., Chen, J., Shi, H., Zhang, X., Liu, J., Shi, D., Huang, Y., Tong, D., Feng, L., 2022. Nucleocytoplasmic shuttling of porcine parvovirus NS1 protein mediated by the CRM1 nuclear export pathway and the importin alpha/beta nuclear import pathway. J. Virol. 96, e0148121.

Chorba, T., Coccia, P., Holman, R.C., Tattersall, P., Anderson, L.J., Sudman, J., Young, N. S., Kurczynski, E., Saarinen, U.M., Moir, R., et al., 1986. The role of parvovirus B19 in aplastic crisis and erythema infectiosum (fifth disease). J. Infect. Dis. 154, 383–393.

Conti, E., Uy, M., Leighton, L., Blobel, G., Kuriyan, J., 1998. Crystallographic analysis of the recognition of a nuclear localization signal by the nuclear import factor karyopherin alpha. Cell 94, 193–204.

Cotmore, S.F., McKie, V.C., Anderson, L.J., Astell, C.R., Tattersall, P., 1986. Identification of the major structural and nonstructural proteins encoded by human parvovirus B19 and mapping of their genes by procaryotic expression of isolated genomic fragments. J. Virol. 60, 548–557.

Deng, X., Dong, Y., Yi, Q., Huang, Y., Zhao, D., Yang, Y., Tijssen, P., Qiu, J., Liu, K., Li, Y., 2013. The determinants for the enzyme activity of human parvovirus B19 phospholipase A2 (PLA2) and its influence on cultured cells. PLoS One 8, e61440.

Di Antonio, V., Palu, G., Alvisi, G., 2021. Live-cell analysis of human cytomegalovirus DNA polymerase holoenzyme assembly by resonance energy transfer methods. Microorganisms 9.

Emsley, P., Lohkamp, B., Scott, W.G., Cowtan, K., 2010. *Features and development of Coot*. Acta crystallographica. Section D, Biol. Crystallograp. 66, 486–501.

Fontes, M.R., Teh, T., Kobe, B., 2000. Structural basis of recognition of monopartite and bipartite nuclear localization sequences by mammalian importin-alpha. J. Mol. Biol. 297, 1183–1194.

Fontes, M.R., Teh, T., Jans, D., Brinkworth, R.I., Kobe, B., 2003. Structural basis for the specificity of bipartite nuclear localization sequence binding by importin-alpha. J. Biol. Chem. 278, 27981–27987.

Gerlitz, G., Livnat, I., Ziv, C., Yarden, O., Bustin, M., Reiner, O., 2007. Migration cues induce chromatin alterations. Traffic 8, 1521–1529.

Ghassabian, H., Falchi, F., Timmoneri, M., Mercorelli, B., Loregian, A., Palu, G., Alvisi, G., 2021. Divide et impera: an In Silico Screening Targeting HCMV ppUL44 Processivity Factor Homodimerization Identifies Small Molecules Inhibiting Viral Replication. Viruses 13.

Gorlich, D., Kostka, S., Kraft, R., Dingwall, C., Laskey, R.A., Hartmann, E., Prehn, S., 1995. Two different subunits of importin cooperate to recognize nuclear localization signals and bind them to the nuclear envelope. Curr. Biol. 5, 383–392.

Gonzalez, A., Mannen, T., Cagatay, T., Fujiwara, A., Matsumura, H., Niesman, A.B., Brautigam, C.A., Chook, Y.M., Yoshizawa, T., 2021. Mechanism of karyopherin-beta2 binding and nuclear import of ALS variants FUS(P525L) and FUS(R495X). Sci. Rep. 11, 3754.

Hoad, M., Roby, J.A., Forwood, J.K., 2021. Structural characterization of the porcine adeno-associated virus Po1 capsid protein binding to the nuclear trafficking protein importin alpha. FEBS Lett. 595, 2793–2804.

Hoad, M., Cross, E.M., Donnelly, C.M., Sarker, S., Roby, J.A., Forwood, J.K., 2023. Structural characterization of porcine adeno-associated virus capsid protein with nuclear trafficking protein importin alpha reveals a bipartite nuclear localization signal. Viruses 15, 315.

Hodel, M.R., Corbett, A.H., Hodel, A.E., 2001. Dissection of a nuclear localization signal. J. Biol. Chem. 276, 1317–1325.

Ihalainen, T.O., Niskanen, E.A., Jylhava, J., Turpeinen, T., Rinne, J., Timonen, J., Vihinen-Ranta, M., 2007. Dynamics and interactions of parvoviral NS1 protein in the nucleus. Cell Microbiol. 9 (8), 1946–1959.
Jakel, S., Albig, W., Kutay, U., Bischoff, F.R., Schwamborn, K., Doenecke, D., Gorlich, D., 1999. The importin beta/importin 7 heterodimer is a functional nuclear import receptor for histone H1. EMBO J. 18, 2411–2423.
Kabsch, W., 2010. *Xds*. Acta crystallographica. Section D, Biol. Crystallograp. 66, 125–132.
Ketkar, H., Yang, L., Wormser, G.P., Wang, P., 2019. Lack of efficacy of ivermectin for prevention of a lethal Zika virus infection in a murine system. Diagn. Microbiol. Infect. Dis. 95, 38–40.
Kosugi, S., Hasebe, M., Entani, T., Takayama, S., Tomita, M., Yanagawa, H., 2008. Design of peptide inhibitors for the importin alpha/beta nuclear import pathway by activity-based profiling. Chem. Biol. 15, 940–949.
Kosugi, S., Hasebe, M., Tomita, M., Yanagawa, H., 2009. Systematic identification of cell cycle-dependent yeast nucleocytoplasmic shuttling proteins by prediction of composite motifs. Proc. Natl. Acad. Sci. U.S.A. 106, 10171–10176.
Lanford, R.E., Butel, J.S., 1984. Construction and characterization of an SV40 mutant defective in nuclear transport of T antigen. Cell 37, 801–813.
Lange, A., Mills, R.E., Lange, C.J., Stewart, M., Devine, S.E., Corbett, A.H., 2007. Classical nuclear localization signals: definition, function, and interaction with importin alpha. J. Biol. Chem. 282, 5101–5105.
Li, Q., Zhang, Z., Zheng, Z., Ke, X., Luo, H., Hu, Q., Wang, H., 2013. Identification and characterization of complex dual nuclear localization signals in human bocavirus NP1: identification and characterization of complex dual nuclear localization signals in human bocavirus NP1. J. Gen. Virol. 94, 1335–1342.
Li, J., Guo, Y., Deng, Y., Hu, L., Li, B., Deng, S., Zhong, J., Xie, L., Shi, S., Hong, X., Zheng, X., Cai, M., Li, M., 2021. Subcellular localization of epstein-barr virus BLLF2 and its underlying mechanisms. Front. Microbiol. 12, 672192.
Luo, Y., Lou, S., Deng, X., Liu, Z., Li, Y., Kleiboeker, S., Qiu, J., 2011. Parvovirus B19 infection of human primary erythroid progenitor cells triggers ATR-Chk1 signaling, which promotes B19 virus replication. J. Virol. 85, 8046–8055.
Luo, Y., Kleiboeker, S., Deng, X., Qiu, J., 2013. Human parvovirus B19 infection causes cell cycle arrest of human erythroid progenitors at late S phase that favors viral DNA replication. J. Virol. 87, 12766–12775.
Lv, C., Liu, W., Wang, B., Dang, R., Qiu, L., Ren, J., Yan, C., Yang, Z., Wang, X., 2018. Ivermectin inhibits DNA polymerase UL42 of pseudorabies virus entrance into the nucleus and proliferation of the virus in vitro and vivo. Antivir. Res. 159, 55–62.
Manaresi, E., Conti, I., Bua, G., Bonvicini, F., Gallinella, G., 2017. A Parvovirus B19 synthetic genome: sequence features and functional competence. Virology 508, 54–62.
Manaresi, E., Gallinella, G., 2019. Advances in the development of antiviral strategies against parvovirus B19. Viruses 11.
Marfori, M., Mynott, A., Ellis, J.J., Mehdi, A.M., Saunders, N.F., Curmi, P.M., Forwood, J. K., Boden, M., Kobe, B., 2011. Molecular basis for specificity of nuclear import and prediction of nuclear localization. Biochim. Biophys. Acta 1813, 1562–1577.
Mastrangelo, E., Pezzullo, M., De Burghgraeve, T., Kaptein, S., Pastorino, B., Dallmeier, K., de Lamballerie, X., Neyts, J., Hanson, A.M., Frick, D.N., Bolognesi, M., Milani, M., 2012. Ivermectin is a potent inhibitor of flavivirus replication specifically targeting NS3 helicase activity: new prospects for an old drug. J. Antimicrob. Chemother. 67, 1884–1894.
Miyatake, H., Sanjoh, A., Murakami, T., Murakami, H., Matsuda, G., Hagiwara, K., Yokoyama, M., Sato, H., Miyamoto, Y., Dohmae, N., Aida, Y., 2016. Molecular mechanism of HIV-1 Vpr for binding to importin-alpha. J. Mol. Biol. 428, 2744–2757.
Moffatt, S., Yaegashi, N., Tada, K., Tanaka, N., Sugamura, K., 1998. Human parvovirus B19 nonstructural (NS1) protein induces apoptosis in erythroid lineage cells. J. Virol. 72, 3018–3028.
Morita, E., Tada, K., Chisaka, H., Asao, H., Sato, H., Yaegashi, N., Sugamura, K., 2001. Human parvovirus B19 induces cell cycle arrest at G(2) phase with accumulation of mitotic cyclins. J. Virol. 75, 7555–7563.
Morita, E., Nakashima, A., Asao, H., Sato, H., Sugamura, K., 2003. Human parvovirus B19 nonstructural protein (NS1) induces cell cycle arrest at G(1) phase. J. Virol. 77, 2915–2921.
Munasinghe, T.S., Edwards, M.R., Tsimbalyuk, S., Vogel, O.A., Smith, K.M., Stewart, M., Foster, J.K., Bosence, L.A., Aragao, D., Roby, J.A., Basler, C.F., Forwood, J.K., 2022. MERS-CoV ORF4b employs an unusual binding mechanism to target IMPalpha and block innate immunity. Nat. Commun. 13, 1604.
Nakada, R., Hirano, H., Matsuura, Y., 2015. Structure of importin-alpha bound to a non-classical nuclear localization signal of the influenza A virus nucleoprotein. Sci. Rep. 5, 15055.
Nakada, R., Hirano, H., Matsuura, Y., 2017. Structural basis for the regulation of nuclear import of Epstein-Barr virus nuclear antigen 1 (EBNA1) by phosphorylation of the nuclear localization signal. Biochem. Biophys. Res. Commun. 484, 113–117.
Nakada, R., Matsuura, Y., 2017. Crystal structure of importin-alpha bound to the nuclear localization signal of Epstein-Barr virus EBNA-LP protein. Protein Sci. 26, 1231–1235.
Ng, I.H.W., Chan, K.W., Tan, M.J.A., Gwee, C.P., Smith, K.M., Jeffress, S.J., Saw, W.G., Swarbrick, C.M.D., Watanabe, S., Jans, D.A., Gruber, G., Forwood, J.K., Vasudevan, S.G., 2019. Zika virus NS5 forms supramolecular nuclear bodies that sequester importin-alpha and modulate the host immune and Pro-inflammatory response in neuronal cells. ACS Infect. Dis. 5, 932–948.
Nuesch, J.P., Tattersall, P., 1993. Nuclear targeting of the parvoviral replicator molecule NS1: evidence for self-association prior to nuclear transport. Virology 196, 637–651.
Ozawa, K., Kurtzman, G., Young, N., 1986. Replication of the B19 parvovirus in human bone marrow cell cultures. Science 233, 883–886.
Patterson, E.I., Dombrovski, A.K., Swarbrick, C.M., Raidal, S.R., Forwood, J.K., 2013. Structural determination of importin alpha in complex with beak and feather disease virus capsid nuclear localization signal. Biochem. Biophys. Res. Commun. 438, 680–685.
Penzes, J.J., Soderlund-Venermo, M., Canuti, M., Eis-Hubinger, A.M., Hughes, J., Cotmore, S.F., Harrach, B., 2020. Reorganizing the family Parvoviridae: a revised taxonomy independent of the canonical approach based on host association. Arch. Virol. 165, 2133–2146.
Pines, J., Hunter, T., 1994. The differential localization of human cyclins A and B is due to a cytoplasmic retention signal in cyclin B. EMBO J. 13, 3772–3781.
Pumroy, R.A., Ke, S., Hart, D.J., Zachariae, U., Cingolani, G., 2015. Molecular determinants for nuclear import of influenza A PB2 by importin alpha isoforms 3 and 7. Structure 23, 374–384.
Qiu, J., Soderlund-Venermo, M., Young, N.S., 2017. Human parvoviruses. Clin. Microbiol. Rev. 30, 43–113.
Raab, U., Beckenlehner, K., Lowin, T., Niller, H.H., Doyle, S., Modrow, S., 2002. NS1 protein of parvovirus B19 interacts directly with DNA sequences of the p6 promoter and with the cellular transcription factors Sp1/Sp3. Virology 293, 86–93.
Raza, S., Shahin, F., Zhai, W., Li, H., Alvisi, G., Yang, K., Chen, X., Chen, Y., Chen, J., Hu, C., Chen, H., Guo, A., 2020. Ivermectin inhibits bovine herpesvirus 1 DNA polymerase nuclear import and interferes with viral replication. Microorganisms 8.
Reggiani, A., Avati, A., Valenti, F., Fasano, E., Bua, G., Manaresi, E., Gallinella, G., 2022. A functional minigenome of parvovirus B19. Viruses 14.
Reis, G., Silva, E., Silva, D.C.M., Thabane, L., Milagres, A.C., Ferreira, T.S., Dos Santos, C. V.Q., Campos, V.H.S., Nogueira, A.M.R., de Almeida, A., Callegari, E.D., Neto, A.D. F., Savassi, L.C.M., Simplicio, M.I.C., Ribeiro, L.B., Oliveira, R., Harari, O., Forrest, J. I., Ruton, H., Sprague, S., McKay, P., Guo, C.M., Rowland-Yeo, K., Guyatt, G.H., Boulware, D.R., Rayner, C.R., Mills, E.J., Investigators, T., 2022. Effect of early treatment with ivermectin among Patients with Covid-19. N. Engl. J. Med. 386, 1721–1731.
Sanchez, J.L., Romero, Z., Quinones, A., Torgeson, K.R., Horton, N.C., 2016. DNA binding and cleavage by the human parvovirus B19 NS1 nuclease domain. Biochemistry 55, 6577–6593.
Sankhala, R.S., Lokareddy, R.K., Cingolani, G., 2016. Divergent evolution of nuclear localization signal sequences in herpesvirus terminase subunits. J. Biol. Chem. 291, 11420–11433.
Sievers, F., Wilm, A., Dineen, D., Gibson, T.J., Karplus, K., Li, W., Lopez, R., McWilliam, H., Remmert, M., Soding, J., Thompson, J.D., Higgins, D.G., 2011. Fast, scalable generation of high-quality protein multiple sequence alignments using Clustal Omega. Mol. Syst. Biol. 7, 539.
Sinigalia, E., Alvisi, G., Mercorelli, B., Coen, D.M., Pari, G.S., Jans, D.A., Ripalti, A., Palu, G., Loregian, A., 2008. Role of homodimerization of human cytomegalovirus DNA polymerase accessory protein UL44 in origin-dependent DNA replication in cells. J. Virol. 82, 12574–12579.
Smith, K.M., Himiari, Z., Tsimbalyuk, S., Forwood, J.K., 2017. Structural basis for importin-alpha binding of the human immunodeficiency virus tat. Sci. Rep. 7, 1650.
Smith, K.M., Di Antonio, V., Bellucci, L., Thomas, D.R., Caporuscio, F., Ciccarese, F., Ghassabian, H., Wagstaff, K.M., Forwood, J.K., Jans, D.A., Palu, G., Alvisi, G., 2018a. Contribution of the residue at position 4 within classical nuclear localization signals to modulating interaction with importins and nuclear targeting. Biochim. Biophys. Acta 1865, 1114–1129.
Smith, K.M., Tsimbalyuk, S., Edwards, M.R., Cross, E.M., Batra, J., Soares da Costa, T.P., Aragao, D., Basler, C.F., Forwood, J.K., 2018b. Structural basis for importin alpha 3 specificity of W proteins in Hendra and Nipah viruses. Nat. Commun. 9, 3703.
Studier, F.W., 2005. Protein production by auto-induction in high density shaking cultures. Protein Expr. Purif. 41, 207–234.
Tay, M.Y., Fraser, J.E., Chan, W.K., Moreland, N.J., Rathore, A.P., Wang, C., Vasudevan, S.G., Jans, D.A., 2013. Nuclear localization of dengue virus (DENV) 1-4 non-structural protein 5; protection against all 4 DENV serotypes by the inhibitor Ivermectin. Antivir. Res. 99, 301–306.
Tay, M.Y., Smith, K., Ng, I.H., Chan, K.W., Zhao, Y., Ooi, E.E., Lescar, J., Luo, D., Jans, D. A., Forwood, J.K., Vasudevan, S.G., 2016. The C-terminal 18 amino acid region of dengue virus NS5 regulates its subcellular localization and contains a conserved arginine residue essential for infectious virus production. PLoS Pathog. 12, e1005886.
Timney, B.L., Raveh, B., Mironska, R., Trivedi, J.M., Kim, S.J., Russel, D., Wente, S.R., Sali, A., Rout, M.P., 2016. Simple rules for passive diffusion through the nuclear pore complex. J. Cell Biol. 215, 57–76.
Trevisan, M., Di Antonio, V., Radeghieri, A., Palu, G., Ghildyal, R., Alvisi, G., 2018. Molecular requirements for self-interaction of the respiratory syncytial virus matrix protein in living mammalian cells. Viruses 10.
Tsujii, A., Miyamoto, Y., Moriyama, T., Tsuchiya, Y., Obuse, C., Mizuguchi, K., Oka, M., Yoneda, Y., 2015. Retinoblastoma-binding protein 4-regulated classical nuclear transport is involved in cellular senescence. J. Biol. Chem. 290, 29375–29388.
UniProt, C., 2021. UniProt: the universal protein knowledgebase in 2021. Nucleic Acids Res. 49, D480–D489.
Wagstaff, K.M., Rawlinson, S.M., Hearps, A.C., Jans, D.A., 2011. An AlphaScreen(R)-based assay for high-throughput screening for specific inhibitors of nuclear import. J. Biomol. Screen 16, 192–200.
Wagstaff, K.M., Sivakumaran, H., Heaton, S.M., Harrich, D., Jans, D.A., 2012. Ivermectin is a specific inhibitor of importin alpha/beta-mediated nuclear import able to inhibit replication of HIV-1 and dengue virus. Biochem. J. 443, 851–856.
Wan, Z., Zhi, N., Wong, S., Keyvanfar, K., Liu, D., Raghavachari, N., Munson, P.J., Su, S., Malide, D., Kajigaya, S., Young, N.S., 2010. Human parvovirus B19 causes cell cycle arrest of human erythroid progenitors via deregulation of the E2F family of transcription factors. J. Clin. Invest. 120, 3530–3544.

Wang, X., Lv, C., Ji, X., Wang, B., Qiu, L., Yang, Z., 2019. Ivermectin treatment inhibits the replication of Porcine circovirus 2 (PCV2) in vitro and mitigates the impact of viral infection in piglets. Virus Res. 263, 80–86.

White, D.G., Woolf, A.D., Mortimer, P.P., Cohen, B.J., Blake, D.R., Bacon, P.A., 1985. Human parvovirus arthropathy. Lancet 1, 419–421.

Wong, S., Zhi, N., Filippone, C., Keyvanfar, K., Kajigaya, S., Brown, K.E., Young, N.S., 2008. Ex vivo-generated CD36+ erythroid progenitors are highly permissive to human parvovirus B19 replication. J. Virol. 82, 2470–2476.

Xu, T.L., Han, Y., Liu, W., Pang, X.Y., Zheng, B., Zhang, Y., Zhou, X.N., 2018. Antivirus effectiveness of ivermectin on dengue virus type 2 in Aedes albopictus. PLoS Neglected Trop. Dis. 12, e0006934.

Yaegashi, N., Shiraishi, H., Takeshita, T., Nakamura, M., Yajima, A., Sugamura, K., 1989. Propagation of human parvovirus B19 in primary culture of erythroid lineage cells derived from fetal liver. J. Virol. 63, 2422–2426.

Yang, S.N.Y., Atkinson, S.C., Fraser, J.E., Wang, C., Maher, B., Roman, N., Forwood, J.K., Wagstaff, K.M., Borg, N.A., Jans, D.A., 2019. Novel flavivirus antiviral that targets the host nuclear transport importin alpha/beta1 heterodimer. Cells 8.

Yang, S.N.Y., Atkinson, S.C., Wang, C., Lee, A., Bogoyevitch, M.A., Borg, N.A., Jans, D.A., 2020. The broad spectrum antiviral ivermectin targets the host nuclear transport importin alpha/beta1 heterodimer. Antivir. Res. 177, 104760.

Zeng, D., Zheng, J., Feng, S., Fan, P., Zhao, D., 2022. Human parvovirus B19 nonstructural protein 1 regulates GATA1 expression via the notch signaling pathway in K562 cell line. Front. Biosci. 27, 261.

Zhi, N., Mills, I.P., Lu, J., Wong, S., Filippone, C., Brown, K.E., 2006. Molecular and functional analyses of a human parvovirus B19 infectious clone demonstrates essential roles for NS1, VP1, and the 11-kilodalton protein in virus replication and infectivity. J. Virol. 80, 5941–5950.

Zou, W., Wang, Z., Xiong, M., Chen, A.Y., Xu, P., Ganaie, S.S., Badawi, Y., Kleiboeker, S., Nishimune, H., Ye, S.Q., Qiu, J., 2018. Human parvovirus B19 utilizes cellular DNA replication machinery for viral DNA replication. J. Virol. 92.